HIGH-PRESSURE ELASTIC PROPERTIES OF MAJOR MATERIALS OF EARTH'S MANTLE FROM FIRST PRINCIPLES

Bijaya B. Karki[1]
Department of Chemical Engineering and Materials Science
Minnesota Supercomputing Institute
University of Minnesota–Twin Cities
Minneapolis, Minnesota, USA

Lars Stixrude
Department of Geological Sciences
University of Michigan
Ann Arbor, Michigan, USA

Renata M. Wentzcovitch
Department of Chemical Engineering and Materials Science
Minnesota Supercomputing Institute
University of Minnesota–Twin Cities
Minneapolis, Minnesota, USA

Abstract. The elasticity of materials is important for our understanding of processes ranging from brittle failure, to flexure, to the propagation of elastic waves. Seismologically revealed structure of the Earth's mantle, including the radial (one-dimensional) profile, lateral heterogeneity, and anisotropy are determined largely by the elasticity of the materials that make up this region. Despite its importance to geophysics, our knowledge of the elasticity of potentially relevant mineral phases at conditions typical of the Earth's mantle is still limited: Measuring the elastic constants at elevated pressure-temperature conditions in the laboratory remains a major challenge. Over the past several years, another approach has been developed based on first-principles quantum mechanical theory. First-principles calculations provide the ideal complement to the laboratory approach because they require no input from experiment; that is, there are no free parameters in the theory. Such calculations have true predictive power and can supply critical information including that which is difficult to measure experimentally. A review of high-pressure theoretical studies of major mantle phases shows a wide diversity of elastic behavior among important tetrahedrally and octahedrally coordinated Mg and Ca silicates and Mg, Ca, Al, and Si oxides. This is particularly apparent in the acoustic anisotropy, which is essential for understanding the relationship between seismically observed anisotropy and mantle flow. The acoustic anisotropy of the phases studied varies from zero to more than 50% and is found to depend on pressure strongly, and in some cases nonmonotonically. For example, the anisotropy in MgO decreases with pressure up to 15 GPa before increasing upon further compression, reaching 50% at a pressure of 130 GPa. Compression also has a strong effect on the elasticity through pressure-induced phase transitions in several systems. For example, the transition from stishovite to $CaCl_2$ structure in silica is accompanied by a discontinuous change in the shear (S) wave velocity that is so large (60%) that it may be observable seismologically. Unifying patterns emerge as well: Eulerian finite strain theory is found to provide a good description of the pressure dependence of the elastic constants for most phases. This is in contrast to an evaluation of Birch's law, which shows that this systematic accounts only roughly for the effect of pressure, composition, and structure on the longitudinal (P) wave velocity. The growing body of theoretical work now allows a detailed comparison with seismological observations. The athermal elastic wave velocities of most important mantle phases are found to be higher than the seismic wave velocities of the mantle by amounts that are consistent with the anticipated effects of temperature and iron content on the P and S wave velocities of the phases studied. An examination of future directions focuses on strategies for extending first-principles studies to more challenging but geophysically relevant situations such as solid solutions, high-temperature conditions, and mineral composites.

1. INTRODUCTION

The behavior of Earth materials at high pressure is central to our understanding of the structure, dynamics, and origin of the Earth. Over the range of conditions that exist within the Earth's mantle, the physical properties of condensed matter depend more strongly on pressure than on other factors such as temperature. The dominant role of pressure, which originates in gravitational self-compression, is reflected in the sublithospheric structure of the Earth, which is spherically symmetric to within a few percent. The response of materials to pressure is governed by an elastic modulus, a relationship embodied, for example, in the Adams-Williamson equation.

In geophysics, we are concerned with the response of

[1]Now at Department of Physics and Astronomy, Louisiana State University, Baton Rouge, Louisiana, USA.

Reviews of Geophysics, 39, 4 / *November 2001*
pages 507–534
8755-1209/01/2000RG000088*$15.00*
Paper number 2000RG000088

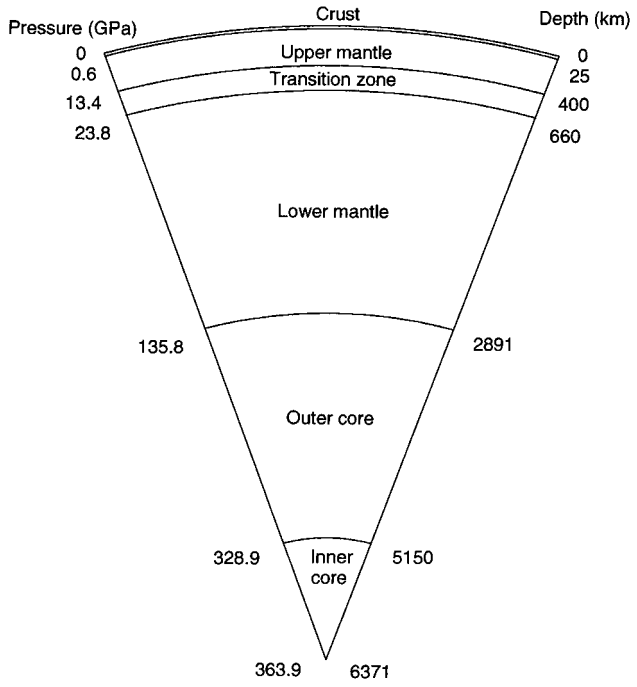

Figure 1. Schematic structure of the Earth's interior.

materials to deviatoric as well as hydrostatic sources of stress. Although deviatoric stresses in the Earth's interior are small compared with the pressure, they are important because of their connection to dynamical processes [*Ruff*, 2001]. Elastic properties govern processes with a characteristic timescale less than the Maxwell relaxation time [e.g., *Jeanloz and Morris*, 1986]

$$\tau_M = \mu/G, \tag{1}$$

where μ is the viscosity, which depends strongly on temperature, and G is the shear modulus. In the lithosphere the viscosity is large and the relaxation time may be longer than the age of the Earth. In this region, knowledge of the elastic constants is important for understanding lithospheric flexure, the onset of brittle failure, and the earthquake source [*Turcotte and Schubert*, 1982; *Aki and Richards*, 1980]. In the mantle the relaxation time is much shorter and is of the order of 1000 years. Here knowledge of the elastic constants is primarily important for understanding the propagation of elastic waves, and normal mode oscillations.

The elastic constants of Earth materials vary substantially over the range of conditions present in the Earth's mantle. With increasing depth, pressure increases rapidly, reaching 136 GPa at the base of the mantle [*Dziewonski and Anderson*, 1981] (Figure 1). The pressure at the base of the mantle is comparable to the bulk modulus of many common minerals and to the pressure scale required to induce significant changes in the electronic structure of materials [*Bukowinski*, 1984; *Stixrude et al*., 1998]. It is natural for us to expect that elastic properties under such extreme conditions are very different from those at ambient conditions. Pressure-induced changes in the elastic constants will reflect changes in the structure and in the nature of bonding due to compression and to phase transformations.

The study of the elastic constants of Earth materials at high pressure provides fruitful ground for an exploration of the foundations of material behavior in the relationship between structure and bonding. The fourth-ranked elastic constant tensor is unusually rich in this regard and reflects the symmetry of the underlying structure. For example, the contrast between periodic and nonperiodic condensed matter is immediately apparent in the elastic anisotropy, a distinction that is not as clear in tensorial properties of lower rank such as the index of refraction, which is isotropic for cubic and nonperiodic materials alike [*Nye*, 1985]. Several studies have used measurements of the elastic constants of particular Earth materials to deepen our understanding of the relationship between elasticity, structure, composition, and bonding [e.g., *Weidner and Vaughan*, 1982].

The study of the elasticity of Earth materials has become increasingly important over the last decade, as contributions from global seismic tomography, seismological investigations of geographically and radially localized regions, mantle discontinuities, analysis of normal modes of oscillations, and other types of studies have revealed the Earth's mantle in unprecedented detail [*Romanowicz*, 1991; *Masters et al*., 1996; *Gaherty et al*., 1996; *Garnero and Helmberger*, 1996; *Shearer*, 2000; *Ishii and Tromp*, 1999]. The spherically averaged (one-dimensional) structure of the interior is affected by solid-solid phase transitions, by variations in temperature with depth (the geotherm), and by any depth-dependent variations in bulk composition that may be present [*Birch*, 1952; *Jeanloz and Thompson*, 1983]. More recent studies have revealed deviations from radially symmetric structure which, though small, are particularly significant because they may be intimately linked to geodynamical processes. For example, anisotropy may be produced by shear deformation associated with mantle flow [*Montagner*, 1998]. Lateral heterogeneity presumably reflects lateral variations in temperature, which are expected in a convecting system, as well as lateral variations in phase assemblage and bulk composition [*Anderson*, 1987; *Robertson and Woodhouse*, 1996; *van der Hilst et al*., 1997; *van der Hilst and Karason*, 1999].

To the extent that the interior behaves elastically, the propagation of seismic waves is determined by the elastic constants of the component materials. Comparison of the elastic properties of potentially relevant minerals with seismic observations permits us to relate those observations to geological process and to the thermal and chemical state of the interior [*Birch*, 1952]. The robustness of this approach is hindered by a number of factors, including anelasticity, the observed attenuation and dispersion of seismic waves within the seismic band [*Anderson and Given*, 1982]. A more serious limitation has been a lack of knowledge of the relevant material

properties at the extreme conditions of the Earth's interior. Major advances in experimental techniques have now made it possible to measure the elasticity of minerals over a considerable pressure and temperature range [*Liebermann and Li*, 1998]. Nevertheless, there are still tremendous challenges in measuring properties such as single-crystal elastic constants in situ.

More recently, an approach complementary to experiment has been developed based on theoretical methods. Recent advances in theory, computational schemes, and hardware have made it possible to solve the fundamental equations of quantum mechanics for large and complex systems. For fundamental, rather than practical, reasons, the equations still cannot be solved exactly, but assumptions can be reduced to a bare minimum. Methods that make only the essential approximations are known as first-principles methods. Here we focus on first-principles methods based on density functional theory [*Hohenberg and Kohn*, 1964; *Kohn and Sham*, 1965], in principle an exact description of ground state electronic and structural properties. These are self-consistent calculations that are completely independent of experiment and make no assumptions regarding the nature of bonding or the electronic structure.

Here we focus on the contributions of first-principles theory to our understanding of mantle elasticity. The subject has not been reviewed before, as the theoretical and computational advances that have made these calculations possible have occurred rapidly over the last decade. The theory can be only briefly described here; the interested reader is referred to more extensive accounts of density functional theory [*Lundqvist and March*, 1987; *Jones and Gunnarsson*, 1989], its application to the solid state [*Heine*, 1970; *Cohen and Heine*, 1970; *Payne et al*., 1992], and theoretical studies in the context of Earth materials [*Wentzcovitch and Price*, 1996; *Stixrude et al*., 1998]. A theme of this review will be that while the calculations are state of the art, they are not exact, and contact with experiment is essential in order to assess the approximations that must be made. A number of good reviews exist on the experimental study of Earth materials at high pressure and high temperature and on the measurement of elastic properties in particular [*Anderson et al*., 1992; *Liebermann and Li*, 1998].

We first describe the basic theory of elasticity in the context of single crystals and polycrystalline aggregates. Then we briefly sketch first-principles methods based on density functional theory and place these in the context of other theoretical methods. Our review of results revolves around the following themes: (1) the effect of pressure on the elastic constants, (2) an understanding of the role of composition and structure in determining the elastic constants of a particular phase, and (3) comparison with the seismic observations of the Earth's mantle. The latter theme highlights issues that have not yet been addressed with first-principles calculations including anelasticity, the deformation of aggregates, and the effect of temperature. A discussion of future prospects focuses on some of these issues and anticipates further progress in our understanding of the mantle.

2. BASIC THEORY OF ELASTICITY

2.1. Strain and Stress Tensors

The elastic constants relate applied external forces, described by the stress tensor, to the resulting deformation, described by the strain tensor. We view a crystal as a homogeneous, anisotropic medium and assume that stress and strain are homogeneous. In the context of geophysics it is sensible to divide the stress into two parts: a prestress, which is nearly hydrostatic throughout most of the Earth's interior, and a further infinitesimal stress of general symmetry. Following *Davies* [1974], we will specialize our development to the case of hydrostatic prestress, noting that this simplification is strictly valid only for those parts of the Earth that cannot support significant deviatoric stresses over geologic time (e.g., the sublithospheric mantle). The strain will also be separated into a large finite deformation associated with the prestress and an infinitesimal strain associated with the incremental stress.

Consider a material point that can be located with respect to Cartesian axes. In the natural or unstressed state, its location is described by the vector **a**. Its position after the application of prestress is denoted by **X** and after the application of the further infinitesimal stress by **x**. The relationship between the prestressed and final positions is given by the displacement

$$u_i = x_i - X_i. \tag{2}$$

We assume that there exists a unique, linear, one-to-one mapping between natural, prestressed, and final coordinates that may be described by the displacement gradients, **u**, **v**, and **w**,

$$x_i - X_i = u_{ij}X_j \tag{3}$$

$$x_i - a_i = v_{ij}a_j = w_{ij}x_j, \tag{4}$$

where the definition of **v** implies a Lagrangian frame of reference and the definition of **w** implies a Eulerian frame.

The displacement gradients contain contributions from deformation and from rotation. For the infinitesimal displacement gradients **u**, these are identified with the symmetric and antisymmetric parts

$$\varepsilon_{ij} = \tfrac{1}{2}(u_{ij} + u_{ji}) \tag{5}$$

$$\omega_{ij} = \tfrac{1}{2}(u_{ij} - u_{ji}), \tag{6}$$

respectively, where ε_{ij} is the infinitesimal or Cauchy strain tensor and ω_{ij} is the rotation tensor. The strain tensor is defined positive for expansion.

The strain associated with prestress will be finite, in

general. In contrast to the infinitesimal case, a unique definition of the finite strain tensor is not possible. The reason is that the displacement gradients **v** and **w** are not frame-indifferent. Consider the change in length of a line element due to the application of prestress,

$$|d\mathbf{x}|^2 - |d\mathbf{a}|^2 = 2e_{ij}dx_i dx_j = 2\eta_{ij}da_i da_j, \tag{7}$$

where the Einstein summation convention has been assumed. These relations define the Eulerian (e) and Lagrangian (η) finite strain tensors. Evaluation of the change in length leads to the following expressions:

$$e_{ij} = \tfrac{1}{2}(w_{ij} + w_{ji} - w_{ij}w_{jk}) \tag{8}$$

$$\eta_{ij} = \tfrac{1}{2}(v_{ij} + v_{ji} + v_{ij}v_{jk}). \tag{9}$$

In the limit of small strains, the nonlinear terms vanish, and these two measures of strain are equivalent, both reducing to the Cauchy strain tensor (equation (5)). However, for finite strains, they differ so that constitutive relations will not be frame-indifferent. This has important implications for the representation and description of physical properties at high pressure including the equation of state [*Knittle and Jeanloz*, 1985].

The stress tensor at a point in a body can be defined through the expression relating the components of the traction **t** acting on the surface elements **dS**,

$$t_i = \sigma_{ij}dS_j. \tag{10}$$

Some care must be taken in the definition [*Wallace*, 1972]. We take the tractions to be those acting on the initial state and the surface elements to be those of the initial, undeformed configuration. In this case, the stress tensor σ_{ij} is the second Pirola-Kirchoff stress [*Dahlen and Tromp*, 1998]. This stress tensor is symmetric, corresponding to vanishing torques acting on the crystal. The components with $i = j$ are the normal components of stress (positive for tensile stresses), and the components with $i \neq j$ are the shear components.

2.2. Definitions of Elastic Constants

The stress tensor can also be defined in terms of the change upon deformation of an appropriate thermodynamic potential. This definition, which will also lead to the expression for the elastic constants, places elasticity within the same framework of other thermodynamic properties of the crystal, such as the equation of state and the entropy. These may all be expressed in terms of the derivatives of the potential with respect to its natural variables [*Wallace*, 1972]. For example, the stress produced by a deformation under isothermal conditions is

$$\sigma_{ij} = \rho\left(\frac{\partial A}{\partial \eta_{ij}}\right)_T, \tag{11}$$

while that produced under isentropic conditions is

$$\sigma_{ij} = \rho\left(\frac{\partial E}{\partial \eta_{ij}}\right)_S, \tag{12}$$

where A is the Helmholtz free energy, E is the internal energy, ρ is the density, and the subscripts on the derivatives indicate that temperature or entropy is to be held constant.

The elastic constants are defined in terms of the Hooke's law relation between stress and strain. The isothermal and adiabatic elastic constants are given by

$$c^T_{ijkl} = \left(\frac{\partial \sigma_{ij}}{\partial \eta_{kl}}\right)_T \tag{13}$$

$$c^S_{ijkl} = \left(\frac{\partial \sigma_{ij}}{\partial \eta_{kl}}\right)_S, \tag{14}$$

respectively. The adiabatic elastic constants are most relevant to seismology, where the timescale of deformation is much shorter than that of thermal diffusion over relevant length scales. Isothermal elastic constants are relevant, for example, in static compression experiments. In the limit of zero temperature and in the absence of zero point motion, the conditions corresponding to most first-principles theoretical calculations, the adiabatic and isothermal elastic constants are identical to each other and are referred to as athermal elastic constants.

It is worth pointing out that other definitions of the elastic constants are possible [*Barron and Klein*, 1965]. In order to distinguish them, the c_{ijkl} may be referred to as the stress-strain coefficients. We may alternatively define

$$C^T_{ijkl} = \rho\left(\frac{\partial^2 A}{\partial \eta_{ij}\partial \eta_{kl}}\right)_T, \tag{15}$$

which is identical to c_{ijkl} only in the absence of prestress. In the case of isotropic prestress (pressure P), the two sets of elastic constants are related by

$$C_{ijkl} = c_{ijkl} + P(\delta_{jl}\delta_{ik} + \delta_{il}\delta_{jk} - \delta_{ij}\delta_{kl}). \tag{16}$$

The C_{ijkl} do not relate stress to strain, in general, and are not directly related to the propagation of elastic waves.

There are 81 independent elastic constants, in general; however, this number is reduced to 21 by the requirement of the Voigt symmetry that c_{ijkl} are symmetric with respect to the interchanges (i, j), (k, l), and (ij, kl). This allows replacement of a pair of Cartesian indices ij by single index α, according to the scheme

ij	α
11	1
22	2
33	3
32 or 23	4
31 or 13	5
21 or 12	6

In Voigt notation the elastic constants thus form a symmetric matrix:

$$c_{ij} = \begin{bmatrix} c_{11} & c_{12} & c_{13} & c_{14} & c_{15} & c_{16} \\ c_{12} & c_{22} & c_{23} & c_{24} & c_{25} & c_{26} \\ c_{13} & c_{23} & c_{33} & c_{34} & c_{35} & c_{36} \\ c_{14} & c_{24} & c_{34} & c_{44} & c_{45} & c_{46} \\ c_{15} & c_{25} & c_{35} & c_{45} & c_{55} & c_{56} \\ c_{16} & c_{26} & c_{36} & c_{46} & c_{56} & c_{66} \end{bmatrix}. \quad (17)$$

The diagonal constants c_{ii} with $i \leq 3$ may be referred to as the longitudinal elastic constants; c_{ii} with $i \geq 4$ may be called the shear elastic constants. Those c_{ij} with $i \neq j < 3$ are referred to as the off-diagonal constants, and finally, c_{ij} with $i \leq 3$ and $j > 3$, which measure the shear strain produced by a longitudinal stress, may be called the mixed elastic constants.

The presence of crystallographic symmetry further reduces the number of independent elastic constants [*Nye*, 1985]. The highest possible symmetry is that of an isotropic material such as a glass or a randomly oriented polycrystalline aggregate, which is fully characterized by two elastic constants. These can be defined as the bulk and shear modulus, K and G, respectively, or in terms of alternative moduli such as the Young's modulus or Lamé parameter, or ratios of moduli, such as the Poisson's ratio. Relationships among these measures are given in a number of sources [*Birch*, 1961]. A cubic crystal is characterized by three constants, c_{11}, c_{12}, and c_{44}. Crystals with lower symmetry will possess a larger number of independent constants, for example, nine for orthorhombic crystals (c_{11}, c_{22}, c_{33}, c_{12}, c_{13}, c_{23}, c_{44}, c_{55}, and c_{66}) and 21 for triclinic crystals (the largest number possible).

Because multiple definitions of the elastic constants exist, some care is required. Examples include the formulation of the Cauchy relations and Born stability criteria. The energy-strain coefficients (C_{ij}) are useful in defining the Cauchy conditions that are valid for a crystal structure in which each atom is located at a center of symmetry and interatomic interaction follows a central-force law. They are

$$\begin{aligned} C_{12} &= C_{66}, \quad C_{13} = C_{55}, \quad C_{23} = C_{44} \\ C_{14} &= C_{56}, \quad C_{25} = C_{46}, \quad C_{36} = C_{45}. \end{aligned} \quad (18)$$

When defined in terms of the stress-strain coefficients (c_{ij}), however, the first three relations involve a pressure term, e.g., $c_{12} - c_{66} - 2P = 0$. The extent to which these conditions are violated measures the importance of noncentral forces in a crystal.

The Born conditions that determine the mechanical stability of a lattice are typically formulated in terms of the C_{ij}. In this case, they are valid only in the limit of vanishing prestress. Several studies [e.g., *Wang et al.*, 1995; *Karki et al.*, 1997e] have demonstrated that the appropriate stability criteria for a stressed lattice are those that are formulated in terms of the stress-strain coefficients and hence are based on enthalpy considerations. Under hydrostatic pressure the three stability criteria for a cubic crystal are

$$c_{11} + 2c_{12} > 0, \quad c_{44} > 0, \quad c_{11} - c_{12} > 0, \quad (19)$$

which are referred to as spinodal, shear, and Born criteria, respectively.

2.3. Finite Strain Theory

Over the pressure regime of the Earth's mantle, elastic moduli may vary by a factor of 5. It has been recognized that in order to describe these large variations, simple Taylor series expansions in pressure generally fail because of their limited radius of convergence. An alternative approach that has found wide application is Eulerian finite strain theory [*Birch*, 1938, 1952; *Davies*, 1974]. The theory is based on a Taylor expansion of the free energy in terms of Eulerian finite strain (equation (8)). For a cubic or isotropic material, the response to pressure is isotropic and the Eulerian finite strain reduces to a scalar. Defining

$$f = -e = (1/2)[(V_0/V)^{2/3} - 1], \quad (20)$$

$$A = af^2 + bf^3 + cf^4 + \ldots, \quad (21)$$

usually truncated at third or fourth order. The volume derivative of A yields the equation of state

$$P = 3K_0 f(1 + 2f)^{5/2}[1 + a_1 f + a_2 f^2] \quad (22)$$

$$a_1 = (3/2)[K_0' - 4] \quad (23)$$

$$a_2 = (3/2)[K_0 K_0'' + K_0'(K_0' - 7) + (143/9)], \quad (24)$$

where subscript 0 denotes values at zero pressure and prime denotes pressure derivatives.

Differentiation of A with respect to strain leads to the expressions for elastic constants [*Davies*, 1974]:

$$c_{ijkl}(f) = (1 + 2f)^{7/2}[c_{ijkl0} + b_1 f + (1/2)b_2 f^2 + \ldots] - P\Delta_{ijkl} \quad (25)$$

$$b_1 = 3K_0(c'_{ijkl0} + \Delta_{ijkl}) - 7c_{ijkl0} \quad (26)$$

$$b_2 = 9K_0^2 c''_{ijkl0} + 3K_0'(b_1 + 7c_{ijkl0}) - 16b_1 - 49c_{ijkl0}, \quad (27)$$

where

$$\Delta_{ijkl} = -\delta_{ij}\delta_{kl} - \delta_{ik}\delta_{jl} - \delta_{il}\delta_{jk} \quad (28)$$

takes on a value of -3 for longitudinal and off-diagonal elastic constants, -1 for the shear constants, and 0 otherwise.

The expression for the elastic constants can be rearranged in a form that is useful for evaluating the convergence properties of the series

$$D_{ijkl}(f) = c_{ijkl0} + b_1 f + \tfrac{1}{2} b_2 f^2 + \ldots, \quad (29)$$

where, by analogy with Birch's definition of the normalized pressure, we have defined

$$D_{ijkl}(f) = \frac{c_{ijkl}(f) + P\Delta_{ijkl}}{(1 + 2f)^{7/2}} \tag{30}$$

as the normalized elastic constants.

2.4. Elastic Wave Velocities

For small vibrations to first order in the displacements u_i about the prestressed state, we can write the equation of motion as

$$\rho \frac{\partial^2 u_i}{\partial t^2} = c_{ijkl} \frac{\partial^2 u_k}{\partial x_j \partial x_l}. \tag{31}$$

The phase velocity (V) and polarization of the three waves along a given propagation direction defined by the unit vector n_i are determined by the condition

$$|c_{ijkl} n_j n_l - \rho V^2 \delta_{ik}| = 0, \tag{32}$$

which is known as the Christoffel equation [*Musgrave*, 1970]. The solutions are of two types: a quasi-longitudinal wave with polarization nearly parallel to the direction of propagation, and two quasi-shear waves with polarization nearly perpendicular to n_i. In seismology the quasi-longitudinal wave is usually referred to as the primary (P) or compressional wave and the quasi-transverse wave is referred to as the secondary (S) or shear wave, the former propagating faster than the latter. Pure longitudinal and shear polarizations are found only in isotropic materials or along special high-symmetry propagation directions in anisotropic materials. For an isotropic, homogeneous material, the P and S wave velocities are related to the elastic moduli by

$$V_P = \sqrt{\frac{K + \frac{4}{3}G}{\rho}}; \qquad V_S = \sqrt{\frac{G}{\rho}}, \tag{33}$$

from which the bulk sound velocity

$$V_B = \sqrt{\frac{K}{\rho}} = \sqrt{V_P^2 - \tfrac{4}{3}V_S^2} \tag{34}$$

can also be defined.

Because the elastic constant tensor is fourth-ranked, all crystals are elastically anisotropic regardless of symmetry. One consequence is that the elastic wave velocities depend on the direction of propagation. The single-crystal azimuthal anisotropy for P and S waves may be defined by the following relations:

$$A_P = \frac{V_{P\max} - V_{P\min}}{V_P}$$

$$A_S = \frac{V_{S\max} - V_{S\min}}{V_S}, \tag{35}$$

where V_P and V_S are the isotropic velocities (that is, averaged over all propagation directions). For the shear waves the polarization anisotropy can be calculated from the difference in velocities of two shear waves ($S1$ and $S2$) propagating in a given direction using

$$A_S^{po} = \frac{V_{S1} - V_{S2}}{V_S}. \tag{36}$$

The maximum polarization anisotropy occurs for the direction in which two shear wave velocities show the largest difference. For cubic crystals, azimuthal and maximum polarization anisotropy are determined by a single anisotropy factor,

$$A = \frac{2(c_{44} - c_s)}{c_{11}}, \tag{37}$$

where $c_s = (c_{11} - c_{12})/2$ [*Karki et al.*, 1997a].

In an anisotropic material the elastic wave fronts generated by a point source will be nonspherical. As a result, the group velocity defined by $V_{Gi} = \partial\omega/\partial k_i$ may differ from the phase velocity defined by $V_i = \omega/k_i$, where ω is the frequency and $\mathbf{k}$ is the phase propagation vector. Seismological measurements are sensitive to the group velocity. With $V_i = Vn_i$, where n_i is the unit vector of the phase velocity, we can relate two velocities [*Helbig*, 1984]:

$$V_{Gi} = Vn_i + k(\partial V/\partial k)n_i + \partial V/\partial n_i. \tag{38}$$

Here the second term, which is collinear with the wave normal, vanishes for a nondispersive medium. In this case, the last term gives the difference between V_i and V_{Gi} and is nonzero for an anisotropic medium. Equation (38) shows that the group velocity surface is simply the tangent surface of the phase velocity surface; and one can be readily calculated from the other [see *Musgrave*, 1970; *Helbig*, 1984]. If the anisotropy is small, group velocity and phase velocity are similar. However, if the anisotropy is large, they may be substantially different. For large anisotropy the group velocity displays triplications that are associated with multiple arrivals for each eigenvector (Figure 2). For example, three distinct P wave arrivals are possible in a given propagation direction.

2.5. Elastic Behavior of Polycrystalline Aggregates

The Earth's mantle and crust are composed of multiphase assemblages in which the elastic constants of adjacent grains may differ widely. For the case of geophysical interest, where the seismic wavelength is much larger than the size of the constituent crystals, the elastic properties of an aggregate can be uniquely calculated from the single-crystal elastic constants if the texture can be specified, that is, the positions, shapes, and orientations of the grains. The texture is typically unknown and, in the absence of direct samples from most of the mantle, is difficult to determine uniquely.

A special case of central geophysical interest is an isotropic monophase aggregate in which the grains are assumed to be randomly oriented but the texture is left otherwise unspecified. Because the texture is only partially known, determination of the elastic moduli is inherently nonunique. Nevertheless, it is possible to con-

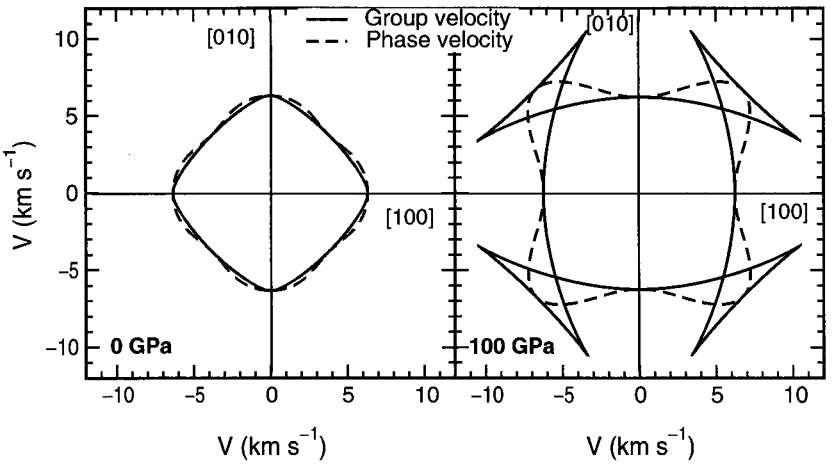

Figure 2. Group velocity (solid curves) and phase velocity (dashed curves) surfaces of *S* waves in MgO in the (001) plane at two pressures. Two velocities are close to each other at zero pressure due to relatively weak anisotropy, but they differ substantially at 100 GPa due to relatively strong anisotropy. For the pressure variation of the anisotropy of MgO, see Figure 12.

struct rigorous bounds. The most commonly used are the Voigt and Reuss bounds, which correspond to conditions of strain and stress continuity, respectively, across grain boundaries [*Hill*, 1952; *Watt et al*., 1976]. The *Hashin and Shtrikman* [1962] bounds are tighter and are widely used for high-symmetry crystals. In the case of cubic crystals the bulk modulus is uniquely defined by

$$K = \tfrac{1}{3}(c_{11} + 2c_{12}). \tag{39}$$

The isotropic shear modulus in the *Hashin and Shtrikman* [1962] averaging scheme is given by

$$G_{\mathrm{HSA}} = \tfrac{1}{2}(G_{\mathrm{HS}+} + G_{\mathrm{HS}-}), \tag{40}$$

where the upper and lower bounds (interchangeable) are

$$G_{\mathrm{HS}+} = c_{44} + 2\left(\frac{5}{c_s - c_{44}} + \frac{18(K + 2c_{44})}{5c_{44}(3K + 4c_{44})}\right) \tag{41}$$

$$G_{\mathrm{HS}-} = c_s + 3\left(\frac{5}{c_{44} - c_s} + \frac{12(K + 2c_s)}{5c_s(3K + 4c_s)}\right), \tag{42}$$

respectively, where $c_s = (c_{11} - c_{12})/2$. Formulas for lower-symmetry crystals have been derived; see *Watt* [1987] for a review.

Bulk anisotropy of monophase aggregates may be caused by lattice-preferred orientation (LPO) of the grains. LPO may develop when the aggregate is subjected to a shear deformation, such as that associated with mantle flow. For example, LPO produced in olivine aggregates in the laboratory has been used to interpret observations of seismic anisotropy in the uppermost mantle [*Christensen and Salisbury*, 1979]. The anisotropy of the aggregate can be no larger than that of the constituent single crystals; often it is a factor of 2–3 smaller depending on the degree of alignment and the details of the texture. Polyphase aggregates may exhibit LPO or a different type of anisotropy due to shape-preferred orientation (SPO). In SPO the anisotropy is due to spatial inhomogeneity in the distribution of phases. For example, an aggregate may consist of layers that are alternately rich in one of two primary phases. If there is no LPO, and if the two phases have different elastic properties, the aggregate will be transversely anisotropic for elastic waves with wavelength much larger than the layer thickness. The solution for this case is well known [*Backus*, 1962] and shows, for example, that *P* waves travel fastest parallel to the layers.

For monophase aggregates the elastic constants of the aggregate, c'_{ijkl}, can be related to those of the single crystal, c_{ijkl}, by [*Mainprice et al*., 2000]

$$c'_{ijkl} = \int a_{im}a_{jn}a_{ko}a_{lp}c_{mnop}f(\mathbf{a})\mathbf{da}, \tag{43}$$

where the elements of the coordinate transformation matrix a_{ij} are the direction cosines that relate crystallographic to sample coordinate systems, and f is the orientation distribution function (ODF), which specifies the volume fraction of crystals oriented according to **a** [*Bunge*, 1982; *Wenk*, 1985]. For the special case of a transversely isotropic medium, the aggregate is characterized by five independent elastic constants. For example, if the single crystals have orthorhombic or higher symmetry and the *c* crystallographic direction of all grains is aligned with a vertical symmetry axis, we have

$$c'_{11} = \tfrac{3}{8}(c_{11} + c_{22}) + \tfrac{1}{4}c_{12} + \tfrac{1}{2}c_{66} \tag{44}$$

$$c'_{33} = c_{33} \tag{45}$$

$$c'_{13} = \tfrac{1}{2}(c_{13} + c_{23}) \tag{46}$$

$$c'_{66} = \tfrac{1}{8}(c_{11} + c_{22}) - \tfrac{1}{4}c_{12} + \tfrac{1}{2}c_{66} \quad (47)$$

$$c'_{44} = \tfrac{1}{2}(c_{44} + c_{55}). \quad (48)$$

2.6. Anelasticity

The response of materials to stress or strain is, in general, not perfectly elastic. In an anelastic material, strain and stress are not in phase. The associated strain-energy losses are expressed in terms of the quality factor Q:

$$\frac{2\pi}{Q} = -\frac{\Delta E}{E}. \quad (49)$$

A number of physical mechanisms may be responsible for dissipation, including motion of dislocations and other defects [*Jackson and Anderson*, 1970; *Karato and Spetzler*, 1990]. In part because different mechanisms are operative at different timescales, the value of Q may depend on frequency. Over the range of frequencies probed in the laboratory (approximately gigahertz for Brillouin scattering and megahertz for ultrasonic techniques), attenuation appears to be sufficiently small that it does not significantly affect measurements of the elastic constants of crystalline solids (dissipation, however, is important in silicate liquids) [*Rivers and Carmichael*, 1987]. At the much lower frequencies probed by seismology, the solid Earth is measurably anelastic; quality factors for shear waves appear to be nearly independent of frequency over most of the seismic band and range from 600 in the lithosphere to 80 in the low-velocity zone to 300 at the base of the mantle [*Masters and Shearer*, 1995]. The quality of volume compression is substantially higher, although it may not be infinite for a discussion of possible bulk attenuation mechanisms. The higher quality of volume compression agrees with laboratory measurements of the equation of state of crystalline solids by static compression (essentially zero frequency), which are consistent with values of the bulk modulus measured by high-frequency techniques [*Bass et al*., 1981; *Duffy et al*., 1995].

Anelasticity entails dispersion (frequency dependence) of elastic wave velocities. For the standard linear solid, the relative magnitude of the dispersion is $\sim 1/Q$ in the modulus, or $\sim 1/2Q$ in the velocity [*Kanamori and Anderson*, 1977]. For a quality factor of 100, typical of the upper mantle, the difference between infinite and zero-frequency elastic wave velocities is 0.5%. Though the effect is small, it is comparable to the magnitude of lateral variations in velocity that are observed in the Earth's mantle. This has important implications for the interpretation of seismic tomography (especially S wave tomography) in terms of lateral variations in temperature, composition, or phase [*Karato*, 1993].

3. THEORETICAL METHODS

It is only recently that first-principles theoretical methods have become widely applicable to the relatively large and complex structures that are characteristic of most Earth materials. Within the theoretical framework a mineral is viewed as an interacting many-particle system of nuclei and electrons. A central goal is the calculation of the ground state electronic and crystallographic structure of the material. This is accomplished by calculating the quantum mechanical total energy of the system and subsequently minimizing that energy with respect to the lattice constants, positions of the nuclei, and the electronic degrees of freedom. One can then derive various physical properties starting from knowledge of the most stable structure of the system; for example, the elastic moduli can be determined from computation of the strain-induced energies or stresses generated by small deformations of the equilibrium lattice [*Ihm*, 1988].

To solve the many-particle problem exactly is impossible; a wide diversity in methodology (ranging from empirical to first-principles) results from the number and types of simplifications and approximations that are needed to obtain solutions with reasonable computational efficiency. First-principles approaches are those that seek to solve the fundamental equations of quantum mechanics with a bare minimum of approximations.

Two types of first-principles methods have appeared in the Earth sciences literature. The extension of Hartree-Fock theory to periodic systems has been used to study a variety of mantle materials, as well as surfaces and defect structures [*Dovesi et al*., 2000]. This method includes one type of many-body interactions between the electrons exactly (exchange) and neglects another completely (correlation). Here we focus on a different method, based on density functional theory, which has found wider application in the study of the Earth's interior. The essence of the theory and some details of its implementation are briefly sketched in the following sections.

3.1. Density Functional Theory

Density functional theory (DFT), originally developed by *Hohenberg and Kohn* [1964] and *Kohn and Sham* [1965], is, in principle, an exact theory of the ground state and allows us to reduce the interacting many-electron problem to a single-electron problem (the nuclei being treated as an adiabatic background). An appealing aspect of the theory is that the central quantity, the charge density, is routinely measured experimentally, for example, by X-ray diffraction. The essence of the theory is that the ground state total energy (and hence the ground state physical properties) of a system is a unique functional of the charge density $n(\mathbf{r})$:

$$E[n(\mathbf{r})] = F[n(\mathbf{r})] + \int V_{\text{ion}}(\mathbf{r})n(\mathbf{r})\, d\mathbf{r}. \quad (50)$$

Here functional $F[n]$ contains the electronic kinetic energy and all the electron-electron interactions and is independent of the external potential, which is usually the Coulomb potential V_{ion} due to ions (or nuclei) plus possibly other external fields. The minimum value of the total energy functional is the ground state energy of the system at the ground state density.

A key to the application of DFT in handling the interacting electron gas was given by *Kohn and Sham* [1965] by splitting up the kinetic energy of a system of interacting electrons into the kinetic energy of noninteracting electrons plus some remainder which can be conveniently incorporated into the exchange-correlation energy. The functional $F[n]$ can be written as

$$F[n(\mathbf{r})] = T[n(\mathbf{r})] + E_{\text{H}}[n(\mathbf{r})] + E_{\text{XC}}[n(\mathbf{r})]. \quad (51)$$

For noninteracting electrons the explicit forms for the kinetic energy and charge density are

$$T[n(\mathbf{r})] = -\frac{\hbar^2}{2m}\sum_{i=1}^{N}\int \psi_i^*(\mathbf{r})\nabla^2\psi_i(\mathbf{r})\, d\mathbf{r} \quad (52)$$

$$n(\mathbf{r}) = \sum_{i=1}^{N} \psi_i^*(\mathbf{r})\psi_i(\mathbf{r}), \quad (53)$$

respectively, where the ψ_i are the single-electronic wave functions. The Hartree energy (Coulomb interaction among electrons) is given by

$$E_{\text{H}}[n(\mathbf{r})] = \frac{1}{2}\int\int \frac{n(\mathbf{r})n(\mathbf{r}')}{|\mathbf{r}-\mathbf{r}'|}\, d\mathbf{r}\, d\mathbf{r}'. \quad (54)$$

The last term, E_{XC}, whose explicit form is not known, is the exchange-correlation energy and contains all the many-body effects in an interacting system.

Using the variational principle implied by properties of the energy functional, one can derive the effective single-electron Schrödinger equation, well known as the Kohn-Sham (KS) equation:

$$\left\{-\frac{\hbar^2}{2m}\nabla^2 + V_{\text{ion}}[n(\mathbf{r})] + V_{\text{H}}[n(\mathbf{r})] + V_{\text{XC}}[n(\mathbf{r})]\right\} \cdot \psi_i(\mathbf{r}) = \varepsilon_i\psi_i(\mathbf{r}), \quad (55)$$

where the Hartree potential is

$$V_{\text{H}}[n(\mathbf{r})] = \int \frac{n(\mathbf{r}')}{|\mathbf{r}-\mathbf{r}'|}\, d\mathbf{r}' \quad (56)$$

and the exchange-correlation potential which contains all the many-body effects is

$$V_{\text{XC}}[n(\mathbf{r})] = \frac{\delta E_{\text{XC}}[n(\mathbf{r})]}{\delta n(\mathbf{r})}. \quad (57)$$

The KS equation constitutes a self-consistent field problem; that is, the self-consistent solutions (electronic wave functions ψ_i and eigenvalues ε_i) can be obtained by iteratively solving the KS equation (equation (55)). Then the total electron density is determined from (53), and hence the total energy E can be computed.

To solve the Kohn-Sham equations exactly requires knowledge of the exact exchange-correlation functional. For the simple case of the uniform electron gas, the explicit expression for the exchange component is known from the Hartree-Fock theory, but the correlation component is known only numerically from quantum Monte Carlo calculations [*Ceperley and Alder*, 1980; *Perdew and Zunger*, 1981]. The charge density in real materials is not uniform, so the exchange-correlation functional cannot be calculated precisely. The local density approximation (LDA) [*Kohn and Sham*, 1965; *Jones and Gunnarsson*, 1989] replaces the exchange-correlation potential at each point **r** by that of a homogeneous electron gas with a density equal to the local density at point **r**.

The LDA works remarkably well for a wide variety of materials; the equation of state, elastic constants, and other properties often agree with experiment to within a few percent. Agreement with laboratory measurements is not perfect, however, and some systematic discrepancies are apparent. In silicates and oxides, LDA tends to overbind; that is, the predicted volume is too small and the elastic moduli is too large compared with experiment. Attempts to improve LDA through consideration of nonlocal corrections have met with some success. The generalized gradient approximation (GGA) [*Perdew et al*., 1996] is a marked improvement over LDA in the case of transition metals [*Bagno et al*., 1989; *Stixrude et al*., 1994]. There is some evidence that GGA improves energetics for silicates and oxides but structures tend to be underbound: The volume calculated with GGA tends to be larger than that measured experimentally [*Hamann*, 1996; *Demuth et al*., 1999; *Oganov et al*., 2001].

3.2. Self-Consistent Methods

Self-consistent methods are those that determine the ground state total energy and the ground state charge density with which it is uniquely associated. These methods will be described in more detail here. They are contrasted with non-self-consistent methods, which do not determine the ground state charge density but typically approximate its form, according to a physical model. These are discussed more fully in other reviews [*Stixrude et al*., 1998]. Examples include Gordon-Kim type approaches (modified electron gas, or MEG, and potential induced breathing, or PIB) in which the charge density consists of overlapping, spherically symmetric, formally charged ions, and Slater-Koster type tight binding methods. Such methods are often referred to as ab initio methods. A distinct class of methods which entails another level of approximation are those based on interatomic potentials. Here the solid is viewed as consisting of atoms or ions, rather than at the fundamental level of nuclei and electrons. The additional approxima-

tions inherent in this approach generally render interatomic potential calculations semiempirical.

There are a number of self-consistent methods for solving the Kohn-Sham equations, and these methods differ from each other mainly in two aspects: (1) inclusion of all electrons or use of pseudopotential approximation, and (2) details of the basis functions (ϕ_j) used to expand the electronic wave functions:

$$\psi_i(\mathbf{r}, \mathbf{k}) = \sum_j b_{i,j}\phi_j(\mathbf{r}, \mathbf{k}), \tag{58}$$

where $b_{i,j}$ are the coefficients and $\mathbf{k}$ is the wave vector.

All electron approaches include the linearized augmented plane wave (LAPW) method [*Jansen and Freeman*, 1984; *Wei and Krakauer*, 1985; *Singh*, 1994]. In LAPW, no approximations are made to the shape of the charge density or the potential. As such, the LAPW is generally accepted to be highly accurate and suitable to all types of crystals irrespective of their bonding nature. The accuracy of the method derives from its basis, which explicitly treats the first-order partitioning of space into near-nucleus regions, where the charge density and its spatial variability are large, and interstitial regions, where the charge density is smaller and varies more gradually. These two regions are delimited by the construction of so-called muffin-tin spheres of radius R^{α}_{MT} centered on each nucleus α. A dual basis set is constructed, consisting of plane waves in the interstitial regions that are matched smoothly to more rapidly varying functions inside the spheres. Other all-electron approaches that have been applied in the Earth sciences include the augmented plane wave (APW) method [*Moruzzi et al*., 1978; *Bukowinski*, 1985] and the full-potential linearized muffin-tin orbital (FP-LMTO) method [*Anderson*, 1975; *Soderlind et al*., 1996].

Representation of the rapidly varying core states makes all-electron calculations relatively intensive computationally. The central idea of the plane wave pseudopotential method (PWPP) is that the precise representation of these states is not essential because they participate little in bonding [*Heine*, 1970; *Pickett*, 1989]. The strong potential due to the nucleus and core electrons is replaced by a weaker, more slowly varying potential with the same scattering properties (the pseudopotential). This approach speeds up calculations substantially because (1) only valence electrons are treated explicitly and (2) the pseudocharge density and potential vary much more slowly in space. The latter feature is particularly important, as it allows one to use plane waves as the basis functions to represent the electronic wave function at each wave vector $\mathbf{k}$:

$$\psi_i(\mathbf{r}, \mathbf{k}) = \sum_G c_{i,\mathbf{k}+\mathbf{G}} \exp\,[i(\mathbf{k} + \mathbf{G}) \cdot \mathbf{r}], \tag{59}$$

where $\mathbf{G}$ is a reciprocal lattice vector. Evaluation of total energies, forces, and stresses with the plane wave basis set is particularly efficient [*Nielsen and Martin*, 1985]. Construction of the pseudopotential is a nonunique process, but differences between different pseudopotentials [*Hamann et al*., 1979; *Vanderbilt*, 1990; *Troullier and Martins*, 1991; *Lee*, 1995], and between PWPP and all electron calculations, are often smaller than the uncertainties due to approximations to the exchange-correlation potential.

An important technical issue is the convergence of the calculations. In either all-electron or PWPP calculations, the two convergence parameters are the number of points in the Brillouin zone (k points) at which the Kohn-Sham equations are solved and the size of the basis set. Convergence with respect to the number of k points is optimized by using special k point meshes [e.g., *Monkhorst and Pack*, 1976]. The size of the basis set is conventionally described either by the maximum kinetic energy of the plane waves included (PWPP) or by the product, $R_{MT}K_{\max}$, of the smallest muffin-tin radius and the largest wave vector (LAPW). An important feature of self-consistent methods is that convergence with respect to the size of the basis is generally smooth, so that convergence tests can be applied with some confidence [*Singh*, 1994].

3.3. Ab Initio Molecular Dynamics

The plane wave pseudopotential approach, which combines accuracy, computational efficiency, and formal simplicity, has developed to the point of being used in the context of molecular dynamics (MD) simulations. Although the original technique was not self-consistent [*Car and Parrinello*, 1985], the methodology evolved rapidly [*Payne et al*., 1992], and self-consistent MD became available in the early 1990s [*Wentzcovitch and Martins*, 1991]. This facilitated the implementation of a variable-cell-shape-MD (VCSMD) formalism [*Wentzcovitch*, 1991] in the context of ab initio calculations [*Wentzcovitch et al*., 1993]. This type of simulation is particularly useful in high-pressure studies. Its flexible periodic boundary conditions can capture dynamically even structural phase transitions under pressure [*Wentzcovitch et al*., 1998a] and is useful in investigation of complex low-symmetry structures typical of the Earth's mantle.

In VCSMD the components of the strain tensor are promoted to dynamical variables together with the rescaled ionic coordinates $\mathbf{q}_i$, where $\mathbf{r}_i = (1 + \varepsilon)\mathbf{q}_i$. The dynamics is then governed by the Lagrangian

$$L = \sum \frac{m_i}{2}\,\dot{\mathbf{q}}_i g \dot{\mathbf{q}}_i + \frac{w}{2}\,\mathrm{Tr}\,(\dot{\varepsilon}\dot{\varepsilon}^T) - E_{\mathrm{KS}}(\mathbf{q}_i, \varepsilon) - PV(\varepsilon), \tag{60}$$

where m_i is the ionic mass, w is the fictitious mass assigned to the simulation cell, and $g = (1 + \varepsilon)^T(1 + \varepsilon)$ is the metric tensor. In the Lagrangian the first and second terms represent the kinetic energies associated with internal and strain variables, respectively, and Kohn-Sham energy and the applied pressure term PV together correspond to the enthalpy which plays the role of the generalized potential energy. The trajectories

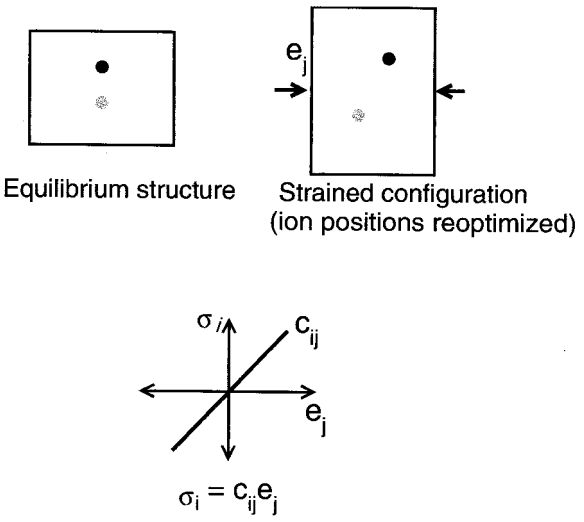

Figure 3. Diagram illustrating the determination of elastic constants by calculating the stress (σ) generated by small deformation of unit cell with strain (ε).

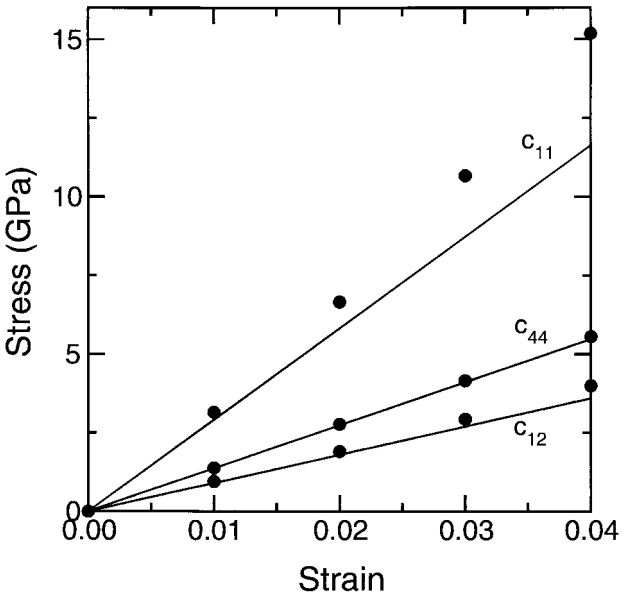

Figure 4. Stress versus strain relations involved in the calculation of three elastic moduli of MgO (taken from *Karki* [1997]). Symbols are the actual calculated points, and lines represent the initial linear slopes (i.e., slopes at origin). Nonlinearity is significant for strains larger than 1% in the case of longitudinal elastic constant (c_{11}), while the effect is weak for other constants.

produced by the resulting equations of motion are invariant with respect to the choice of simulation cell vectors, preserve the relation between strain and stress, and hence conserve the space group symmetry. It was this latter technique that prompted the wide application of the PWPP method to the structurally complex problems involved in mineralogical high-pressure studies [*Wentzcovitch et al.*, 1993, 1995a, 1995b].

3.4. Determination of Elastic Constants

In essence, the determination of the elastic constants proceeds as follows (see Figure 3): At a given pressure (or volume) the crystal structure is first fully optimized, and then the lattice is slightly deformed by applying a small strain. The stress in the strained configuration is calculated, and the values of the elastic constants follow from the linear stress-strain relation

$$\sigma_{ij} = c_{ijkl} e_{kl}. \tag{61}$$

For cubic crystals a single strain of monoclinic symmetry is sufficient to determine all the independent elastic constants [*Karki et al.*, 1997a]. For lower-symmetry structures, such as orthorhombic forsterite or perovskite, four strains of different symmetry are applied [*Karki et al.*, 1997c]. The elastic constants may also be computed from the strain-energy density. If the strains are chosen to be volume conserving,

$$\frac{\Delta E}{V} = \frac{1}{2} c_{ijkl} e_{ij} e_{kl}. \tag{62}$$

This is useful in LAPW calculations where computation of the stress tensor is difficult [*Cohen*, 1991; *Steinle-Neumann et al.*, 1999].

There are two important factors to be taken into account in determining elastic constants. First, the ionic positions need to be reoptimized in the strained lattice in order to incorporate any couplings between strains and vibrational modes in the crystal [*Nastar and Willaime*, 1995]. The effects of the coupling are particularly large in the presence of soft vibrational modes, as in the case of silica in the vicinity of the stishovite to $CaCl_2$ structure transition, which is discussed further later [*Cohen*, 1992; *Karki et al.*, 1997b, 1997d]. Second, the elastic constants need to be calculated in the appropriate limit of zero strain. At finite strain, higher-order terms in the stress-strain relationship become important, which are governed by higher-order elastic constants corresponding to third and higher strain derivatives of the energy [e.g., *Wallace*, 1972]. To calculate the elastic constants in the linear regime, strains of different magnitude or sign are applied (Figure 4), and the zero-strain limit is determined by extrapolation or interpolation. It is this linear regime that is most relevant in geophysics.

4. ELASTICITY OF MINERALS

First-principles methods are a powerful way of investigating the elasticity of Earth materials at very high pressures. Recent work has included studies of many of the major Mg-silicate polymorphs including those of Mg_2SiO_4 [*da Silva et al.*, 1997; *Kiefer et al.*, 1997; *Kiefer et al.*, 2001], of $MgSiO_3$ stoichiometries [*Wentzcovitch et al.*, 1995a; *Karki et al.*, 1997c; *Wentzcovitch et al.*, 1998b; *da Silva et al.*, 1999], and of $CaSiO_3$ perovskite [*Sherman*,

1993; *Karki and Crain*, 1998a]. Also investigated have been the oxides MgO [*Karki et al*., 1997a, 1999]; CaO [*Karki and Crain*, 1998b]; SiO_2 [*Cohen*, 1991; *Karki et al*., 1997d]; and Al_2O_3 [*Duan et al*., 1999]. Of the minerals thought to be major constituents of the mantle, only the elastic constants of the pyroxene and garnet phases have not yet been examined theoretically, although the structure and compression mechanisms of enstatite have been investigated [*Wentzcovitch et al*., 1995b]. The elasticity calculations to date have primarily been performed by using ab initio MD as a technique for efficient minimization of stresses and forces in the strained configurations.

While approximations in the first-principles calculations have been reduced to a minimum, the calculations are not exact. This makes comparison with available experimental data essential. The comparison allows us to evaluate the quality of the assumptions that we are forced to make (primarily the form of the exchange-correlation potential) and points the way toward future improvements to the theory. The complementary nature of first-principles theory and experiment is worth emphasizing: The theory has no free parameters and there is no input from experimental data. Because the first-principles calculations are independent of experiment, favorable comparisons between the two approaches can lend confidence to each. We review all extant first-principles calculations of the elastic constants of mantle materials and compare these with available experimental data. Following is a discussion of the patterns which emerge from the theoretical results, focusing on the effect of pressure on the elastic moduli including the elastic anisotropy and the appearance of elastic instabilities and the influence of changes in crystallographic structure and chemical composition on the elastic properties. We further compare the first-principles results with seismological investigations of the Earth's mantle.

4.1. Comparison With Experiment

A summary of calculated athermal elastic constants and their pressure derivatives are compared with experimental results in Table 1. The athermal theoretical elastic constants are expected to be somewhat larger than those measured experimentally at ambient conditions because the effects of temperature and zero-point motion are ignored. Recent theoretical calculations that include the effects of lattice vibrations [*Karki et al*., 1999] show that these amount to a few percent at room temperature. The local density approximation (LDA) to the exchange-correlation potential is also expected to have a systematic effect: It tends to overbind structures; that is, the elastic moduli tend to be overestimated although there are few exceptions, for example, c_{44} of MgO [*Karki et al*., 1997a]. Overall, first-principles theory represents a substantial improvement over the predictions of more approximate theories, such as those based on simplified semiempirical and ab initio models (Table 1).

The results produced by different pseudopotential calculations differ from each other and from those of all electron LAPW calculations. This arises from the nonuniqueness of the pseudopotential and the additional approximations that its construction entails. In the case of MgO the calculations of *Karki et al*. [1997a] underestimate the elastic moduli of MgO as they overestimate the volume. Later results by *Karki et al*. [1999] using different pseudopotentials are more consistent with all-electron calculations [*Mehl et al*., 1988] and with experimental data. In the case of $MgSiO_3$ perovskite, much of the difference between the two sets of the elastic moduli [*Karki et al*., 1997c; *Wentzcovitch et al*., 1998b] can be accounted for by differences in the pseudopotentials used in the calculations. The results of *Oganov et al*. [2001], however, differ substantially from the other two sets because they used the generalized gradient approximation that tends to underbind structure and underestimate the elastic moduli (see Table 1). The differences between the two pseudopotential results with LDA are similar in magnitude to those seen in MgO, as are the differences with respect to the all-electron result [*Stixrude and Cohen*, 1993]. The size of the errors in all cases is comparable to the LDA error.

4.2. Effect of Pressure

4.2.1. Elastic moduli. The effect of pressure on the elastic constants of all major mantle minerals is large, as much as a factor of 5 over the regime of the Earth's mantle. This means that experimental or theoretical results at ambient pressure cannot be used to reliably estimate elasticity at mantle pressures. This is particularly true because the effect of pressure is much larger for certain types of elastic constants than for others (e.g., Figure 5): The pressure-induced variations in the longitudinal elastic constants are relatively large ($c'_{ij0} = 5–10$), compared with those for the shear and off-diagonal constants ($c'_{ij0} = 0.5–4$) (see Table 1).

Finite strain theory [*Birch*, 1938, 1952; *Davies*, 1974] can be used to understand the range of values of c'_{ij0} that are found for longitudinal, off-diagonal, and shear elastic constants. Expansions in the Eulerian finite strain are known to provide rapidly convergent descriptions of isothermal compression (P-V equation of state) to large strains. This success can be understood by recognizing that the coefficients of higher-order terms are small [*Jeanloz*, 1988]. For example, the second-order truncation of the equation of state (i.e., setting $a_1 = 0$ in equation (22)) yields $K'_0 = 4$. First-principles calculations show that K'_0 spans the range of 4–4.5 for several oxides and silicates. This implies that the coefficient a_1 should be small and that the third-order Birch-Murnaghan equation should be adequate for most materials. Truncation at second order of the anisotropic generalization of the Eulerian finite strain expansion ($b_1 = 0$ in equation (25)) leads to the following relation for the pressure derivatives of the elastic constants:

TABLE 1. Calculated Athermal Elastic Moduli (M) and Their Pressure Derivatives (M') at Zero Pressure of Earth Minerals in Comparison With Experiments[a]

Method,[b] *Source*[c]	*Moduli*	c_{11}	c_{22}	c_{33}	c_{44}	c_{55}	c_{66}	c_{12}	c_{13}	c_{23}	K	G
						Forsterite						
PWPP, 1	M	367	220	233	78	89	91	78	79	81	141	89
	M'	7.68	5.30	5.61	1.53	1.34	1.69	3.38	3.46	3.54	4.32	1.44
Exp, 2	M	328	200	235	65	81	81	64	69	74	129	81
	M'	7.22	5.42	5.57	2.01	1.46	2.16	3.59	3.62	2.94	4.12	1.4
						Wadsleyite						
PWPP, 3	M	377	374	289	108	117	109	89	103	108	181	115
	M'	6.16	5.87	6.96	0.87	0.78	2.06	4.01	2.93	3.49	4.34	1.16
Exp, 4	M	371	373	272	111	123	103	66	95	105	170	115
	M'										4.3	1.4
						Ringwoodite						
PWPP, 5	M	361			134			118			199	129
	M'	6.32			0.82			3.18			4.19	1.12
Exp, 6	M	327			126			112			184	119
	M'										4.2	1.73
						$MgSiO_3$ Ilmenite						
PWPP, 7	M	477		392	121	−28[d]	−16[e]	153	89		222	144
	M'	6.0		5.7	2.2	−0.4	0.3	3.5	3.9		4.5	1.6
Exp, 8	M	472		382	106	−27	−24	168	70		212	132
						$MgSiO_3$ Perovskite						
PWPP, 9	M	493	523	460	201	183	147	135	145	158	260	174
	M'	5.15	6.56	6.70	1.98	1.44	1.91	3.33	2.55	2.73	4.02	1.65
PWPP, 10	M	485	560	474	200	176	155	130	136	144	259	179
PWPP, 11	M	444	484	408	194	172	131	110	126	136	231	162
Exp, 12	M	482	537	485	204	186	147	144	147	146	264	177
	M'										4.0	1.8
PIB, 13	M	548	551	441	241	253	139	54	153	175	256	196
RI, 14	M	460	506	378	162	159	112	139	184	177	260	140
						$CaSiO_3$ Perovskite						
PWPP, 15	M	374			225			167			236	165
	M'	7.28			2.47			3.0			4.42	2.46
PHF, 16	M	367			290			222			307	209
Exp, 17	M										232	
	M'										4.8	
						MgO						
PWPP, 18	M	291			137			90			157	121
PWPP, 19	M	323			152			92			169	135
	M'	9.0			1.05			1.91			4.27	2.39
Exp, 20	M	297			156			95			162	131
	M'	9.17			1.11			1.61			4.13	2.53
PIB, 21	M	310			188			119			182	143
MEG, 22	M	226			142			142			170	86
						CaO						
PWPP, 23	M	241			77			52			115	83
	M'	10.11			0.45			1.67			4.48	1.78
Exp, 24	M	223			81			59			114	81
	M'	8.7			0.74			1.71			4.05	1.81
PIB, 25	M	206			66			50			102	71
MEG, 22	M	207			97			97			134	77
						Stishovite						
PWPP, 26	M	456		734	254		325	216	195		310	223
	M'	···		4.31	2.09		3.30	···	2.03		4.24	1.72
LAPW, 27	M	452		807				242	221		324	
Exp, 28	M	453		776	252		302	211	203		312	226
	M'										4.3	1.8
PIB, 29	M	623		977	347		424	450	146		412	277

TABLE 1. (continued)

Method,[b] *Source*[c]	*Moduli*	c_{11}	c_{22}	c_{33}	c_{44}	c_{55}	c_{66}	c_{12}	c_{13}	c_{23}	K	G
					Al_2O_3							
PWPP, 30	M	502		501	157	−19[d]		161	125		258	168
	M′	5.52		5.10	2.03	0.19		3.09	3.57		4.06	1.44
Exp, 31	M	498		502	147	−23		163	117		255	163
	M′	6.17		5.00	2.24	0.13		3.28	3.56		4.30	1.64
PIB, 29	M	540		455	157	−48		157	130		263	170

[a]The pressure dependence of c_{11} and c_{12} of stishovite can be represented by $(c_{11} + c_{12})/2 = 336 + 5.32P$ and $(c_{11} - c_{12})/2 = 120[1 - (P/47)^{3.5}]$, where P is pressure, in gigapascals [*Stixrude*, 1999].

[b]Abbreviations are PWPP, plane wave pseudopotential; PIB, potential induced breathing; RI, rigid ion; PHF, periodic Hartree Fock; MEG, modified electron gas; and LAPW, linearized augmented plane wave.

[c]Sources are 1, *da Silva et al*. [1997]; 2, *Yoneda and Morioka* [1992] and *Zha et al*. [1996]; 3, *Kiefer et al*. [2001]; 4, *Zha et al*. [1997] and *Li et al*. [1998]; 5, *Kiefer et al*. [1997]; 6, *Weidner et al*. [1984] and *Rigden et al*. [1992]; 7, *da Silva et al*. [1999]; 8, *Weidner and Ito* [1985]; 9, *Karki et al*. [1997c]; 10, *Wentzcovitch et al*. [1998b]; 11, with the generalized gradient approximation [*Oganov et al*., 2001]; 12, *Yaganeh-Haeri* [1994] and *Sinelnikov et al*. [1998]; 13, *Cohen* [1987b]; 14, *Matsui et al*. [1987]; 15, *Karki and Crain* [1998a]; 16, *Sherman* [1993]; 17, *Wang et al*. [1996]; 18, *Karki et al*. [1997a]; 19, *Karki et al*. [1999]; 20, *Sinogeikin and Bass* [1999]; 21, *Isaak et al*. [1990]; 22, *Cohen and Gordon* [1976]; 23, *Karki and Crain* [1998b]; 24, *Chang and Graham* [1977]; 25, *Mehl et al*. [1986]; 26, *Karki et al*. [1997d]; 27, *Cohen* [1991, 1992]; 28, *Weidner et al*. [1982] and *Andrault et al*. [1998]; 29, *Cohen* [1987a]; 30, *Duan et al*. [1999]; 31, *Geiske and Barsch* [1968].

[d]Mixed modulus c_{14}.

[e]Mixed modulus c_{25}.

$$c'_{ij0} = \frac{7}{3}\frac{c_{ij0}}{K_0} - \Delta_{ij}. \quad (63)$$

This results in three sets of c'_{ij0}: one for longitudinal moduli, another for off-diagonal and shear, and a third for mixed elastic constants (Figure 6). For silicates and oxides considered, it is found that the first-principles pressure derivatives fall near the expected trends, which account for the greater pressure derivatives of the longitudinal moduli, intermediate values for off-diagonal and shear, and smallest pressure derivatives for the

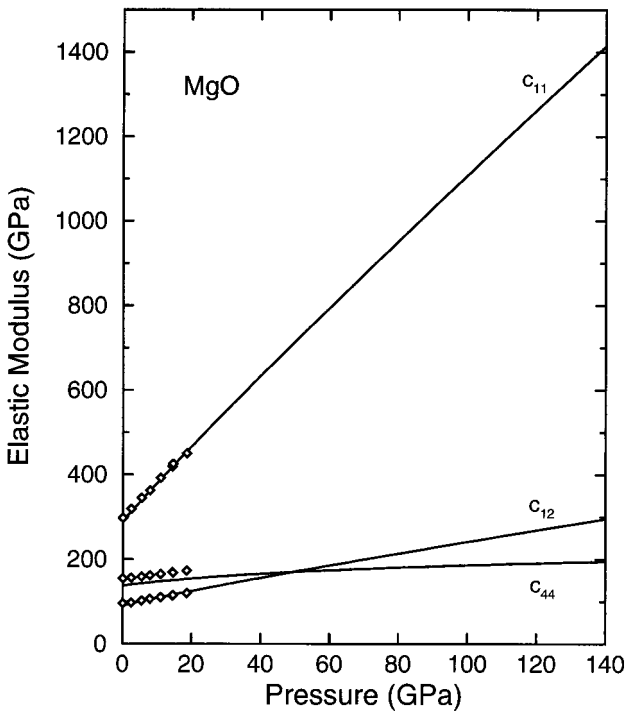

Figure 5. Three elastic moduli, namely, c_{11}, c_{12}, and c_{44}, of MgO in its face-centered cubic structure. The existing low-pressure experimental data (to 19 GPa [*Sinogeikin and Bass*, 1999]) shown by symbols are well reproduced by theory [*Karki et al*., 1997a].

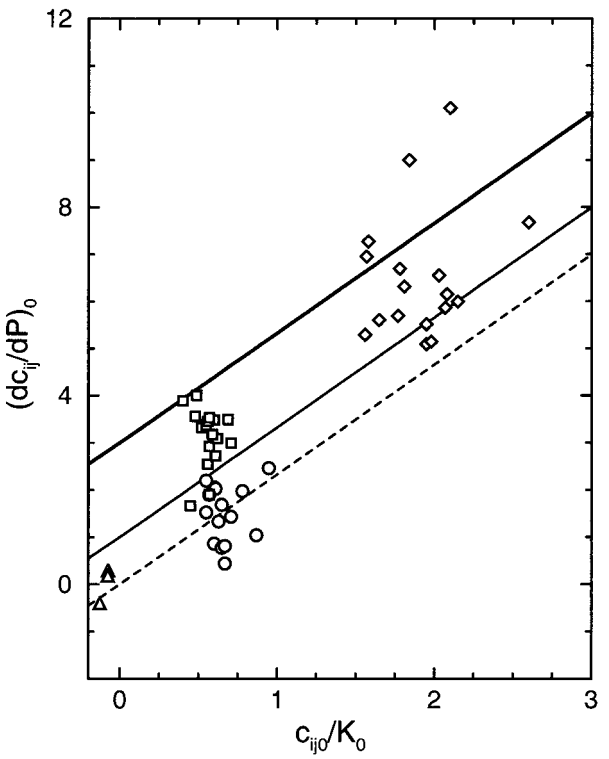

Figure 6. Zero-pressure derivatives for longitudinal constants (bold line) and for off-diagonal and shear constants (thin line), and for mixed elastic constants (dashed line) implied by the second-order finite strain theory. First-principle values for all the minerals considered are denoted by symbols: diamonds, longitudinal constants; squares, off-diagonal constants; circles, shear constants; and triangles, mixed constants.

mixed moduli. Of the patterns apparent in these results, only the systematically larger values of the off-diagonal pressure derivatives as compared with the shear are not explained. Therefore one expects that the third-order expansion will be sufficient for describing the effect of pressure on the elastic constants in many materials.

First-principles results allow us to evaluate the convergence properties of the Eulerian finite strain description of the elastic constants. For example, the normalized elastic constants of perovskite are found to depend nearly linearly on finite strain over the pressure range 0–140 GPa (Figure 7). The finite strain expansion truncated at the linear term fits the theoretical elastic constants to within 1%. For the off-diagonal moduli (c_{12}, c_{13}, and c_{23}) the first-principles results appear to resolve a small nonlinear term. Normalized elastic constants that vary nearly linearly with finite strain have been found for most other materials studied as well, suggesting that the finite strain expansions of c_{ij} converge rapidly and that third-order equations are, in general, sufficient. Exceptions include c_{11} and c_{12} of stishovite, which show highly nonlinear behavior (due to the elastic instability associated with the stishovite-to-$CaCl_2$ phase transition). It is worth emphasizing that Taylor series expansions in variables other than the finite strain will not converge as rapidly, in general. For example, Taylor series expansions in the pressure are not appropriate: In MgO, extrapolations linear and quadratic in pressure differ by 100% at relatively low pressures (60 GPa) [*Karki et al.*, 1997a].

An alternative representation of the effect of compression on elastic properties is provided by Birch's law [*Birch*, 1961]:

$$V_P = a(\bar{M}) + b\rho, \tag{64}$$

implying a unique relationship between compressional velocity and density for materials of the same mean atomic weight $\bar{M}$. Birch's law refers only to the effective longitudinal wave velocity of isotropic polycrystals, not to the individual elastic constants. Birch speculated that the above velocity density relations should hold for all changes of density irrespective of their origin, i.e., whether caused by variations in pressure, temperature, phase, or bulk composition.

The first-principles results show that the effect of pressure on the elastic wave velocities of major mantle minerals does not follow Birch's law (Figure 8). In particular, the calculated velocity profiles of several minerals are nonlinear in density. This behavior is in contrast to that of simpler ionic materials such as halite or sylvite, which obey Birch's law over a wide range of compression [*Campbell and Heinz*, 1992]. The violation of Birch's law in silicates and oxides may be related to the nature of bonding in these materials. Unlike in the alkali halides, noncentral covalent and many-body forces are important, as evidenced by violations of the Cauchy conditions. While Birch's law is not obeyed, it does appear to provide a qualitative description of the effect of pressure in silicates and oxides. In particular, the Birch's law slope is similar in most cases to the average slope of theoretical results in density-velocity space.

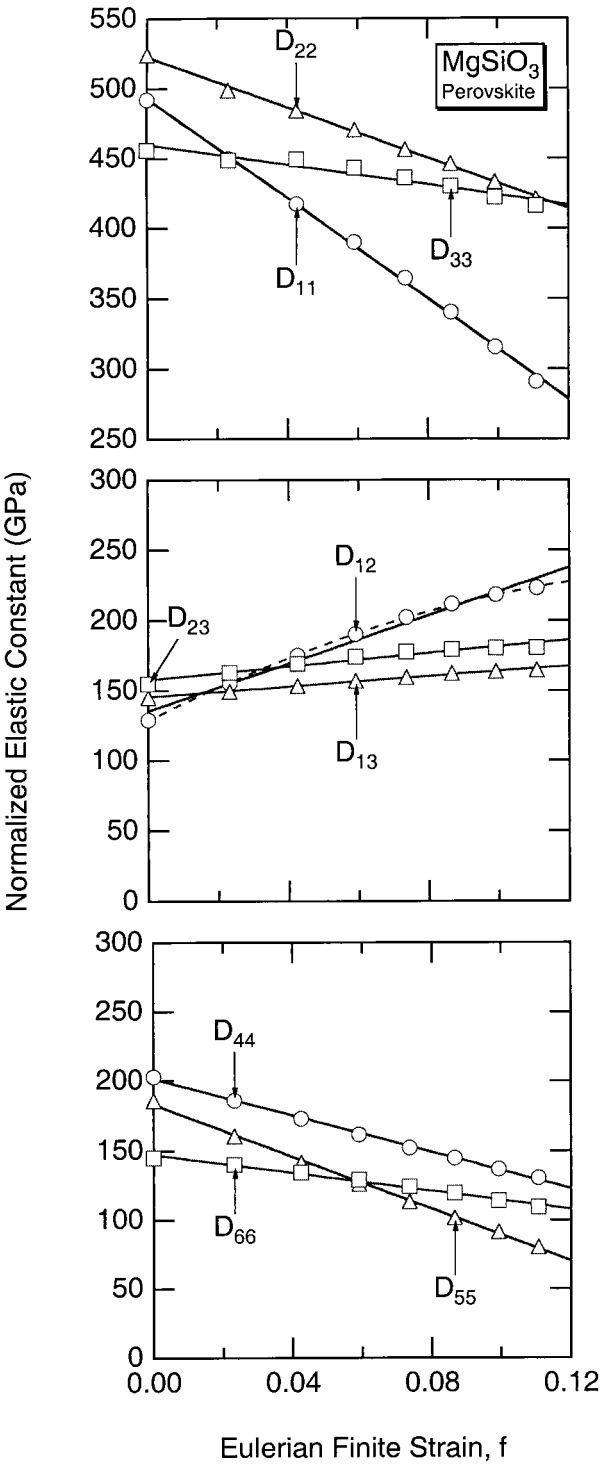

Figure 7. Finite strain dependence of the normalized elastic constants of $MgSiO_3$ perovskite. Labels use Voigt notation. The observed linear variations (solid lines) suggest that the third-order finite strain theory can well account for the pressure effects on most cases.

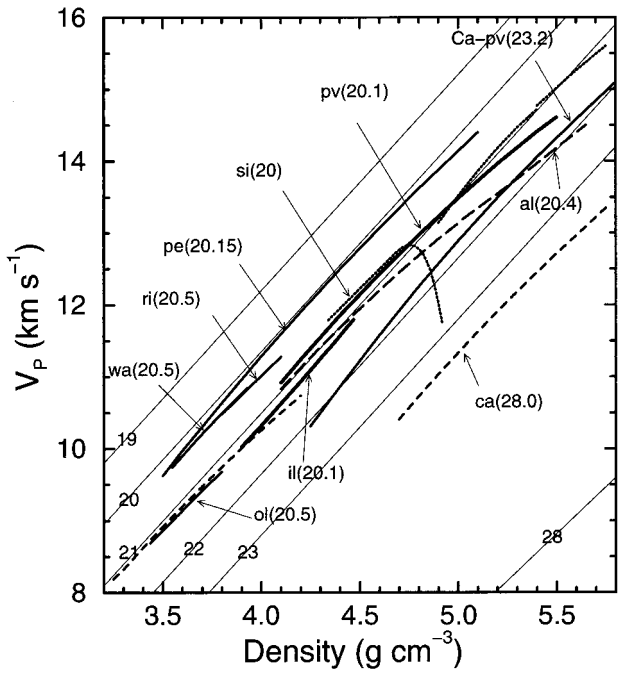

Figure 8. Calculated compressional velocity versus density for several minerals, ol, forsterite; wa, wadsleyite; ri, ringwoodite; il, $MgSiO_3$ ilmenite; pv, $MgSiO_3$ perovskite; Ca-pv, $CaSiO_3$ perovskite; pe, MgO; ca, B1 and B2 phases of CaO; si, three phases (stishovite, $CaCl_2$, and columbite) of SiO_2; and al, corundum and Rh_2O_3(II) phase of Al_2O_3. The mean atomic weight of each phase is shown by the number in parentheses. Thin lines are those estimated by Birch's law for different $\bar{M}$ shown by numbers.

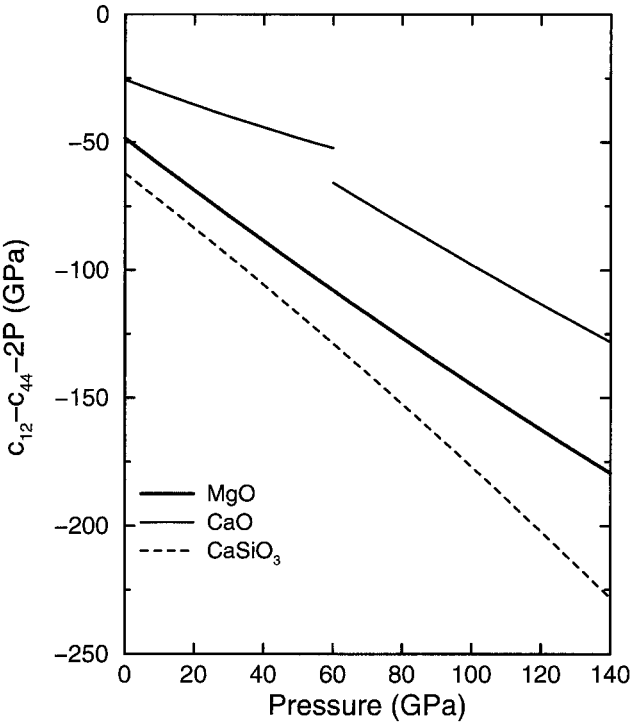

Figure 9. Pressure dependence of the Cauchy violation in cubic crystals, MgO, CaO (B1 and B2 phases), and $CaSiO_3$ perovskite [*Karki*, 1997]. All three systems show stronger violation at higher pressures.

The Cauchy conditions are only relevant for MgO, CaO, and cubic $CaSiO_3$ perovskite. The value of $c_{12} - c_{44} - 2P$ for these materials is found to be large and negative and to increase in magnitude with increasing pressure (Figure 9). The strong violation of the Cauchy conditions in these minerals requires an important contribution from noncentral (many-body) forces that increases with pressure. The potential-induced breathing model appears to capture the essential physics, as this simplified model predicts correctly the Cauchy violation in the alkaline Earth oxides [*Isaak et al.*, 1990; *Mehl et al.*, 1986]. The relevant many-body force arises from a spherically symmetric breathing of the oxygen ion in response to strain-induced variations in the Madelung potential at the oxygen site.

Rigorous bounds on the effective moduli of isotropic polycrystalline aggregates can be determined once the single-crystal elastic constant tensor is known [*Watt et al.*, 1976]. We find that for most silicates and oxides over the pressure range of the mantle, the Hashin-Shtrikman bounds differ by less than 2% for the shear modulus and by less than 0.5% for the bulk modulus. The Voigt-Reuss bounds are substantially broader, but the Voigt-Reuss-Hill average generally falls within the Hashin-Shtrikman bounds and agrees closely with the average of the Hashin-Shtrikman bounds (Figure 10). The difference between the bounds depends on the magnitude of the anisotropy, which may change substantially with pressure. The width of the bounds is large only where the anisotropy is unusually large (e.g., $A_S > 50\%$). For example, the condition $c_{11} - c_{12} = 0$ not only makes the anisotropy of SiO_2 diverge in the vicinity of the stishovite-to-$CaCl_2$ phase transition but also causes the lower bound on the shear modulus to vanish [*Karki et al.*, 1997d] (see Table 2). In MgO (Figure 10) and the B1 phase of CaO, the bounds on the shear modulus are relatively wide at high pressure where the anisotropy of these phases is large [*Karki et al.*, 1997a; *Karki and Crain*, 1998b]. In such situations the Hashin-Shtrikman and Voigt-Reuss-Hill averaged values also differ significantly: by 1% in MgO at 140 GPa, by 4% in CaO at 60 GPa, and by 15% in stishovite at 46 GPa. In such cases the HS bounds are preferred.

4.2.2. Instabilities. In most cases, elastic constants increase monotonically with increasing pressure. However, in several cases, elastic constants or combinations of elastic constants may decrease with increasing pressure and may vanish, implying an elastic instability. The analysis of elastic instabilities plays an important role in the theoretical understanding of phase transitions [*Salje*, 1990]. We may divide the elastic instabilities found in mantle materials into two groups. The first type is directly responsible for equilibrium phase transitions; an example is the vanishing of $c_{11} - c_{12}$ at the stisho-

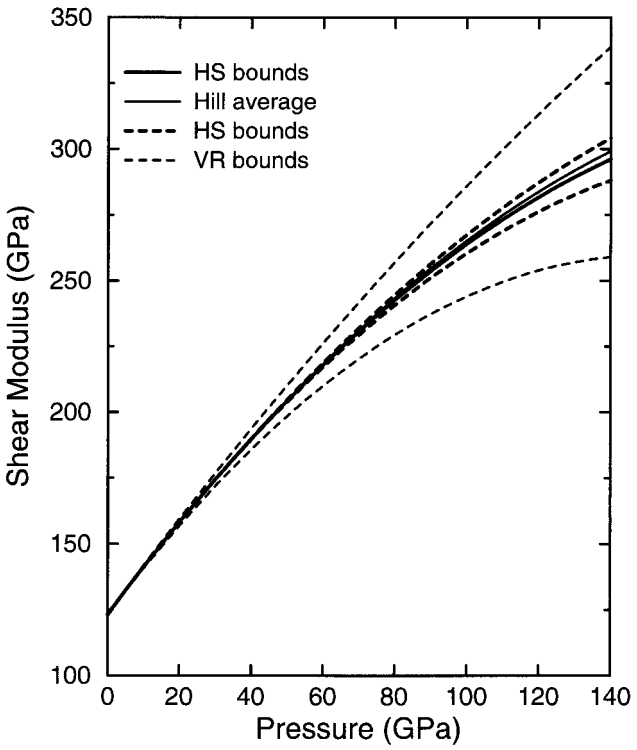

Figure 10. Comparison between the Voigt-Reuss-Hill and Hashin-Shtrikman averaging schemes for the shear modulus of MgO at high pressure [*Karki et al*., 1997a]. Two types of averages agree closely with each other, although Voigt and Reuss bounds are much broader than the Hashin-Shtrikman bounds at high pressure.

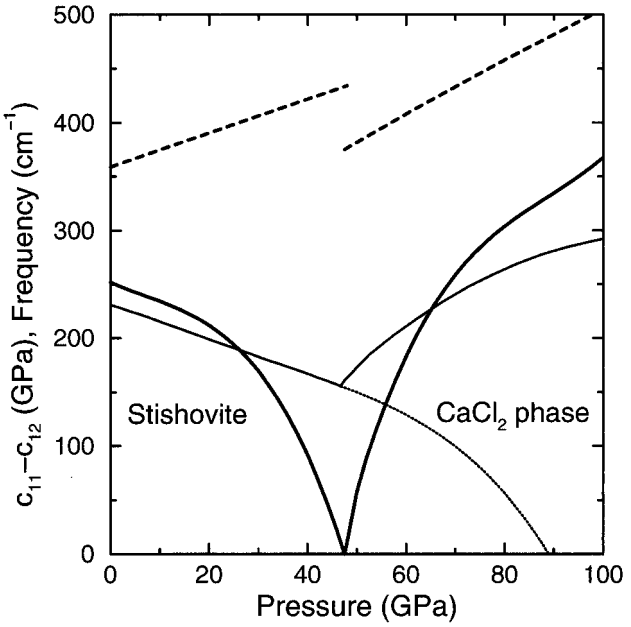

Figure 11. Pressure dependence of $c_{11} - c_{12}$ (bold curve indicates with ionic positions reoptimized in the deformed unit cell, and dashed lines indicate without any ionic relaxation) of stishovite (rutile phase) and $CaCl_2$ phase of SiO_2. Low-frequency Raman modes (B_{1g} for rutile and A_g for $CaCl_2$ phase) are shown by thin curves. The results are taken from *Karki et al*. [1997b].

vite-to-$CaCl_2$ structure transition in silica [*Cohen*, 1992; *Karki et al*., 1997b]. The second type is more common and is found outside the stability field of the mineral. Elastic instabilities of this type may be associated with metastable transformations. Examples are the instabilities in diamond structure of Si [*Mizushima et al*., 1994], zinc-blende structure of SiC [*Tang and Yip*, 1995], B1 phase of MgO and CaO [*Karki et al*., 1997e], corundum and Rh_2O_3(II) phases of Al_2O_3 [*Duan et al*., 1999], and forsterite [*da Silva et al*., 1997].

Silica provides an excellent example of a pressure-induced elastic instability that can precisely be linked to a phase transformation [*Cohen*, 1992; *Karki et al*., 1997b, 1997d]. In stishovite, c_{11} increases slowly with pressure up to 40 GPa and then decreases on further compression, whereas c_{12} grows at an increasing rate, thereby causing $c_{11} - c_{12}$ to vanish at ~47 GPa (the pressure of the stishovite-to-$CaCl_2$ transition), where the tetragonal shear modulus of the $CaCl_2$ phase also vanishes (Figure 11). The $c_{11} - c_{12} = 0$ instability arises from a strong coupling between a shear strain of orthorhombic symmetry in the a-b plane and the soft B_{1g} mode in stishovite or A_g mode in $CaCl_2$ phase. The strain provides a deformation path that relates the lattices of the two structures, whereas the B_{1g} mode involves a rotation of SiO_6 octahedra around the c axis that relates the two structures. The coupling between strain and vibrational mode is strong: The calculated modulus $c_{11} - c_{12}$ does not soften around 47 GPa unless the ions are reoptimized (allowed to relax) in the deformed lattice (Figure 11). While the frequency of the B_{1g} mode is softened considerably by 47 GPa, it does not vanish until much higher pressures (86 GPa), well beyond the stability field

TABLE 2. Voigt-Reuss-Hill Versus Hashin-Shtrikman Isotropic Bulk and Shear Moduli for Three Phases of SiO_2 [*Karki et al*., 1997d][a]

P	K_{VRH}	G_{VRH}	K_{HS}	G_{HS}
		Stishovite		
0	312 ± 5	225 ± 12	312 ± 1	226 ± 2
20	390 ± 3	244 ± 25	390 ± .8	246 ± 6
40	479 ± 2	226 ± 65	478 ± .7	233 ± 28
46	507 ± 1.5	149 ± 142	507 ± .7	132 ± 116
		$CaCl_2$ Phase		
50	505 ± 16	266 ± 47	508 ± 7	267 ± 22
60	521 ± 13	306 ± 31	523 ± 5	305 ± 12
80	586 ± 6.3	350 ± 22	586 ± 2.2	349 ± 7.2
100	654 ± 5.5	380 ± 21	655 ± 1.8	379 ± 6.7
		Columbite Phase		
100	696 ± .5	371 ± 5	696 ± .1	371 ± 1.2
120	760 ± .5	395 ± 6	760 ± .1	395 ± 1.4
140	830 ± .4	413 ± 7	830 ± .1	413 ± 1.8

[a]The plus or minus signs represent the bounds on moduli.

of stishovite. The frequency of the A_g mode of $CaCl_2$ phase increases with increasing pressure.

In MgO and CaO, c_{44} of the B1 phase is shown to increase slowly with increasing pressure and then to soften, vanishing at approximately 1400 and 180 GPa, respectively [*Karki et al*., 1997e]. It can be shown that the shear instability implied by the violation of the $c_{44} > 0$ stability criterion is a deformation path between the face-centered cubic (B1) and simple cubic (B2) structures. However, the B1-B2 phase transition in these materials takes place at a pressure much lower than that of the elastic instability. The softening of c_{44} may be taken as a precursor of the B1-B2 phase transition [*Karki et al*., 1997e]. Other materials that show softening and vanishing of elastic constants at pressures much higher than the limit of their thermodynamic stability fields include forsterite (two shear constants, c_{55} and c_{66}, decrease with pressure beyond 40 and 90 GPa, respectively, and c_{55} vanishes at about 170 GPa [*da Silva et al*., 1997]) and corundum (c_{66} decreases with increasing pressure beyond 250 GPa). For the Rh_2O_3(II) phase of Al_2O_3, c_{55} decreases with increasing pressure beyond 150 GPa, implying a shear instability at a higher pressure [*Duan et al*., 1999].

4.2.3. Anisotropy. As was discussed above, different elastic constants vary with pressure at different rates. One consequence of this is that the elastic anisotropy is, in general, a function of pressure. In some cases, not only the magnitude but also the sense of anisotropy may change significantly with increasing pressure; that is, the directions of fastest and slowest propagation directions may be reversed upon compression.

MgO is a good example of strongly pressure dependent anisotropy. Its anisotropy at first decreases with increasing pressure, vanishes near 15 GPa, and then increases upon further compression [*Karki et al*., 1997b, 1999]. The magnitude of the anisotropy becomes very large at pressures similar to those near the base of the mantle ($A_s \approx 50\%$ at 135 GPa); see Figure 12. The anisotropy factor A (equation (37)) changes sign at ~15 GPa with the consequence that the sense of anisotropy is reversed. The sign of A is in turn determined by the ratio of c_s to c_{44}, which exceeds unity only above 15 GPa. At this pressure the direction of fastest S wave propagation changes from [100], with velocity $\sqrt{c_{44}/\rho}$, to [110], with velocity $\sqrt{c_s/\rho}$ [*Karki et al*., 1997b]. Similar behavior is seen in the case of ringwoodite (Figure 13). The theoretically predicted behavior of MgO is consistent with most experimental observations including those of *Duffy et al*. [1995], *Sinogeikin and Bass* [1999], and the lower-pressure data of *Zha et al*. [2000]. At higher pressures, theory diverges substantially from the data of *Zha et al*. [2000], who found that MgO remains essentially isotropic at pressures greater than 20 GPa.

Other oxides including CaO, Al_2O_3, and SiO_2 are also highly anisotropic. The anisotropy of SiO_2 is the largest in this group and varies most rapidly with increasing pressure (Figure 12). The anisotropy of stishovite dramatically increases near the transition to the $CaCl_2$ structure ($A_s \approx 175\%$). The $CaCl_2$ phase also shows substantial anisotropy ($A_s \approx 75\%$) near the transition pressure. This behavior is attributed to the shear instability associated with the vanishing of $c_{11} - c_{12}$ at the phase transition. The columbite phase of silica (also known as α-PbO_2 structure) is less anisotropic than the lower-pressure structures. The B1 phase of CaO shows increasing anisotropy, which reaches a maximum as the B1-B2 transition is approached (90% A_S at 60 GPa). This is due to softening of c_{44} [*Karki and Crain*, 1998b]. The anisotropy of the corundum phase is found to decrease with pressure up to 50 GPa and then increase slowly [*Duan et al*., 1999]. In contrast, the anisotropy of the Rh_2O_3(II) phase of alumina is relatively large ($A_s \approx 20\%$ at 80 GPa) and increases with compression. The fast and slow propagation directions also change with pressure in Al_2O_3 and SiO_2 but not in CaO, for which they are fixed by the condition $c_{44}/c_s < 1$, which is satisfied at all pressures.

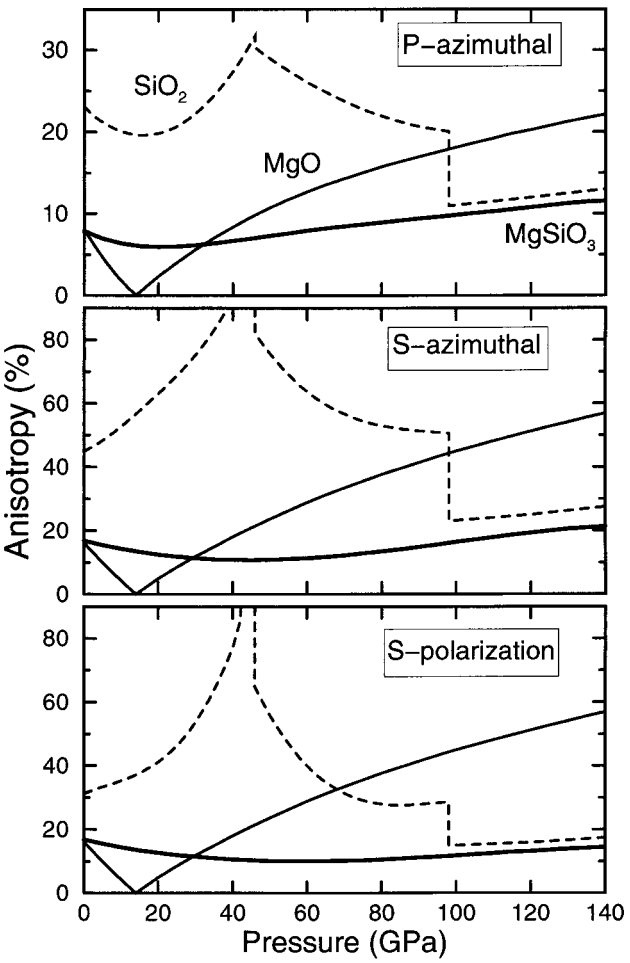

Figure 12. Single-crystal anisotropy (P azimuthal and S azimuthal, i.e., variations with propagation direction; and S polarization, i.e., variation with polarization for a given direction) of $MgSiO_3$ perovskite [*Karki et al*., 1997c], MgO [*Karki et al*., 1997a], and SiO_2 [*Karki et al*., 1997d].

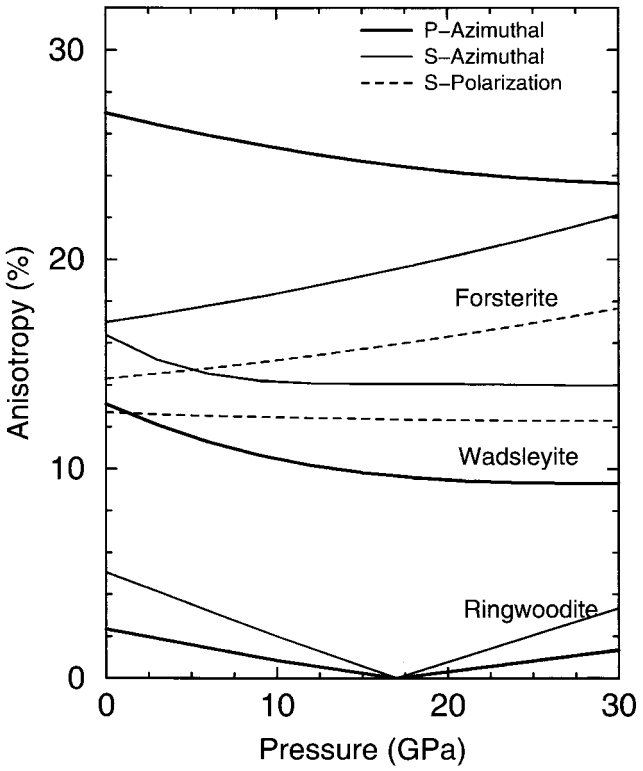

Figure 13. Single-crystal anisotropy (P azimuthal, S azimuthal, and S polarization) of the Mg_2SiO_4 polymorphs: forsterite [*da Silva et al*., 1997], wadsleyite [*Kiefer et al*., 2001], and ringwoodite [*Kiefer et al*., 1997].

In $MgSiO_3$ perovskite the anisotropy at first decreases with increasing pressure to approximately 30 GPa (Figure 12) and then increases, showing changes in the extremal propagation directions [*Karki et al*., 1997c; *Wentzcovitch et al*., 1998b]. For example, the direction of slowest P wave propagation is [001] at 0 GPa but [100] at 140 GPa. This behavior can be understood in terms of the ratio of the longitudinal moduli: $c_{11}/c_{33} > 1$ at 0 GPa but $c_{11}/c_{33} < 1$ at 140 GPa (Figure 7). In contrast, the anisotropy of $CaSiO_3$ perovskite rapidly decreases with increasing pressure from its high initial value (40% A_S), while the extremal propagation directions remain unchanged since $c_{44}/c_s > 1$ at all pressures [*Karki and Crain*, 1998b].

Both theory [*da Silva et al*., 1997; *Kiefer et al*., 2001] and experiments [*Zha et al*., 1996, 1997, 1998] show that the anisotropy of forsterite and wadsleyite varies by only a few percent without any change in the fast and slow directions over the pressure range 0–30 GPa (Figure 13). Similarly, the anisotropy of $MgSiO_3$ ilmenite decreases slightly under compression and remains large (20% A_S at 25 GPa) compared with other minerals of the upper mantle and transition zone [*da Silva et al*., 1999]. The small values of c_{14} and c_{25} in ilmenite lead to a weak transverse anisotropy of ilmenite about the vertical (z) axis and also imply a slight difference between the large anisotropy about the x and y axes. The extremal propagation directions also change with pressure, as determined by the pressure dependence of c_{14} and c_{25}.

4.3. Effect of Structure and Composition

There has been substantial interest in establishing systematic patterns in the effects of crystal structure and composition on the elastic constants [*Duffy and Anderson*, 1989; *Anderson et al*., 1992]. The systematics based on Birch's law (equation (64)) are not well obeyed by first-principles results (Figure 8). Discrepancies are primarily of two types: (1) Results for isochemical polymorphs do not generally fall along the same trend, and (2) results for some minerals do not lie near the curve appropriate for their mean atomic weight. For example, results for forsterite and Mg wadsleyite are nearly coincident and fall near the appropriate curve ($\bar{M} = 20$), as expected from Birch's law, but results for ringwoodite are discrepant, defining a distinct trend that lies near the curve corresponding to $\bar{M} = 21$. Most minerals fall along curves that correspond to a mean atomic weight that is within one unit of the actual value. Notable exceptions are the CaO polymorphs: Results for the B1 and B2 phases of CaO fall along very different trends, both of which, moreover, lie far from the line corresponding to the mean atomic weight of this material ($\bar{M} = 28$). This discrepancy had been noted before in the case of B1 CaO [*Birch*, 1961]. Birch's law is not generally useful in a quantitative sense for estimating the effects of phase transformations on V_P. For example, the change in V_P at the forsterite-to-wadsleyite transition is found to be 0.84 km s^{-1} in the first-principles calculations, as compared with the value that would be derived by using Birch's law to relate the density contrast to the velocity contrast: 0.28 km s^{-1}.

The failure of simple systematics such as Birch's law is perhaps not surprising given the complexity of the problem. In the case of polymorphic phase transitions, we must expect a change not only in density, but also in bonding and crystallographic symmetry. This means that the number of independent elastic constants, as well as their magnitude and pressure dependence, will change in general. Pressure-induced phase transitions are accompanied by significant changes in the isotropic properties (V_P and V_S) as well as in the anisotropy (the magnitude and character). Consider the Mg_2SiO_4 system in which forsterite and wadsleyite are characterized by nine elastic constants, whereas ringwoodite has three (Figure 14). Even the two orthorhombic phases show very different patterns of anisotropy: In forsterite, $c_{11} > c_{33} \approx c_{22}$, whereas in wadsleyite $c_{11} \approx c_{22} > c_{33}$. The P wave anisotropy of wadsleyite is a factor of 2 smaller than that of forsterite; the anisotropy of ringwoodite is much weaker still. The P and S velocities are found to increase by 10–12% at the forsterite-to-wadsleyite transition and by 2–3% at the wadsleyite-to-ringwoodite transition.

In some cases, it is possible to rationalize in a simple way the effect of crystallographic structure on the elas-

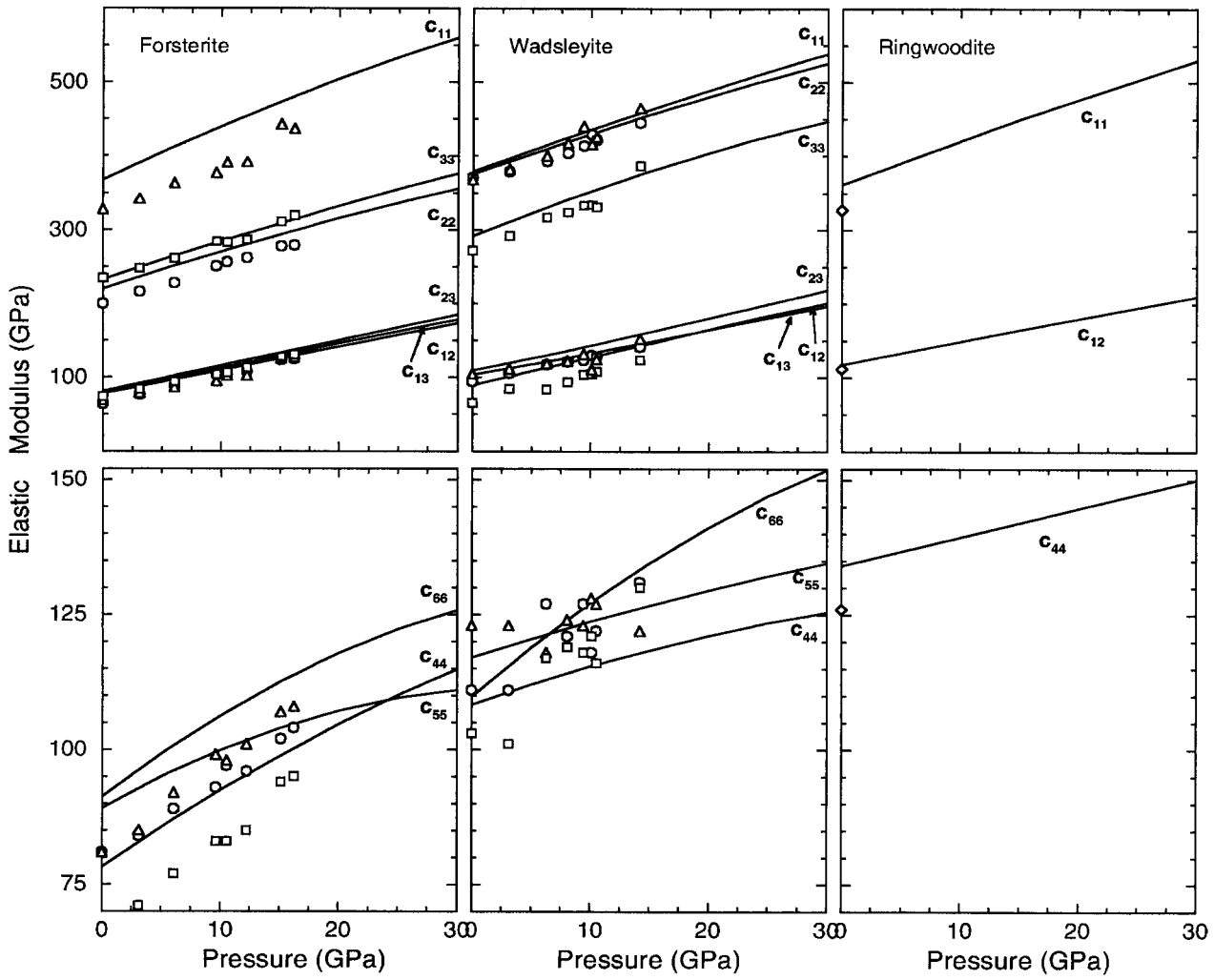

Figure 14. Elastic moduli of the Mg_2SiO_4 polymorphs. Lines indicate theory [*da Silva et al*., 1997; *Kiefer et al*., 1997, 2001]. Symbols indicate the experimental data [*Weidner et al*., 1984; *Yoneda and Morioka*, 1992; *Zha et al*., 1996, 1997].

ticity of isochemical polymorphs. For example, in $MgSiO_3$ the isotropic wave velocities increase substantially (V_S by 20%) across the ilmenite-to-perovskite transition, while the anisotropy drops by a factor of 2. The stiffer perovskite structure results from the complete three-dimensional network of corner sharing SiO_6 octahedra. The Si octahedron is relatively incompressible with a polyhedral bulk modulus [*Hazen and Finger*, 1979] of 330 GPa [*Karki et al*., 1997c]. In contrast, ilmenite is a layered structure in which planes of edge-sharing Si octahedra alternate regularly along the *c* axis with much softer Mg octahedra (polyhedral bulk modulus of 172 GPa [*Karki et al*., 2000]). This arrangement accounts for the lesser isotropic moduli in ilmenite and for its large anisotropy: Compression along *c* is relatively easy and is accommodated mostly by the Mg octahedra, while compression along *a* and *b* can only take place by compressing Si and Mg polyhedra by similar amounts.

The effect of composition on isostructural series may also be substantial. For example, the elastic moduli of B1 MgO are larger than those of B1 CaO at all pressures, and the pressure dependencies of moduli also differ substantially between the two oxides; for example, c_{11} of CaO (B1 phase) increases much more rapidly with pressure than that of MgO. Qualitatively, the lesser moduli in CaO can be related to the greater volume of this compound as compared with MgO. The perovskites provide an interesting contrast. In this structure the volume is set primarily by the Si-O bond length. As a result, the difference in mean atomic volume between Ca- and Mg-silicate perovskites is smaller than would be expected on the basis of the difference in ionic radii of Mg and Ca. The difference in volume is also related to differences in octahedral rotation which lowers the symmetry of Mg-silicate perovskite. The isotropic moduli of $CaSiO_3$ are smaller than those of $MgSiO_3$ perovskite at zero pressure, but they increase more rapidly with increasing pressure. For example, the shear modulus of

$CaSiO_3$ perovskite overtakes that of Mg perovskite at 20 GPa. This may be understood in terms of the increasing importance of short-range repulsion between the larger cation (Ca) and its surrounding oxygens at high pressure.

Corundum and ilmenite are related by a chemical substitution (Tschermak substitution) that replaces alternating layers of Al octahedra with Mg and Si octahedra. Despite the similar structure of these two minerals, they have very different elasticity: In ilmenite, c_{11} is much larger than c_{33}, whereas in corundum, c_{11} and c_{33} are similar throughout the pressure range of stability (Table 1). The greater anisotropy of ilmenite is due to the alternating occupation of the octahedral layers by Mg and Si. As also discussed above, this leads to a relatively compressible c axis and greater resistance to compression in the plane of the layers [*Karki et al*., 2000; *Weidner and Ito*, 1985].

4.4. Comparisons With Seismological Observations

The elastic properties of the major Earth forming minerals predicted by first-principles theory are of substantial geophysical significance. Comparisons of the calculated elastic properties with those of the Earth's interior as determined seismologically lead to a better understanding of the origin of one-dimensional and laterally heterogeneous mantle structure. Moreover, the predicted elastic anisotropy of component minerals can be used to understand the origin of the seismic anisotropy. The comparison is limited by our current lack of knowledge of the effect of temperature on mineral elasticity at the relevant pressures. The point of view adopted here is that the effect of pressure on the elastic properties is predominant, with temperature playing a secondary role. However, a more precise interpretation demands information regarding the thermal and compositional contributions, for example, the effect of iron content.

4.4.1. Isotropic wave velocities. The properties of the Mg_2SiO_4 polymorphs are compared with the seismic profiles of the upper mantle and transition zone in Figure 15. The velocities of forsterite are nearly parallel to the seismic profiles between 200 and 410 km depth and are shifted upward by approximately 7 and 13% for P and S waves, respectively [*da Silva et al*., 1997]. This discrepancy is expected and is due primarily to the effects of temperature, since the theoretical calculations are athermal. A more detailed comparison between theory and seismology requires computations of the elastic wave velocities at high temperature that have not yet been performed. It will also be important to understand the effects of composition (in the mantle, olivine contains a significant amount of fayalite component) and other phases including pyroxene and garnet. Comparisons at greater depth show similar patterns. The P and S velocities of wadsleyite are 12 and 20% larger, respectively, than the properties of the mantle near 410 km depth, and the differences decrease rapidly at greater depths due to steep seismic gradients in the transition zone, which are due in part to phase transformations among other phases including pyroxene and garnet that occur over this range. The velocity profiles of ringwoodite remain parallel to and are 8 and 9% higher than the seismic profiles over the depth range that this mineral is expected to occur in the mantle [*Kiefer et al*., 1997].

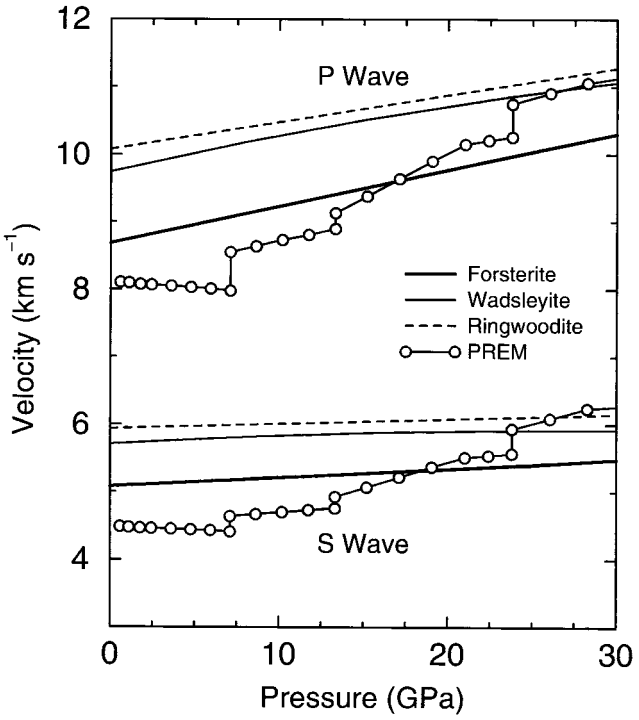

Figure 15. Comparisons of the calculated longitudinal (P) and shear (S) wave velocities of Mg_2SiO_4 polymorphs [*da Silva et al*., 1997; *Kiefer et al*., 2001, 1997], with the seismic data of the upper mantle and transition zone given by the preliminary reference Earth model (PREM) [*Dziewonski and Anderson*, 1981].

The transition from olivine to wadsleyite is thought to be responsible for the seismic discontinuity near 410 km depth. The changes in P and S wave velocities associated with this transition according to theory are 10 and 12%, in good agreement with experimental measurements [*Li et al*., 1998]. A number of authors have compared the change in velocity due to the transition with the magnitude of the velocity discontinuity determined seismologically [*Weidner*, 1985; *Zha et al*., 1996; *Fujisawa*, 1998; *Li et al*., 1998]. However, the seismological value is uncertain in part because it is model-dependent and in part because of real geographic variability in the Earth; seismological estimates range from 2.6 to 3.9% for the discontinuity in V_P and from 3.6 to 6.7% for the discontinuity in V_S. Another important issue may be the apparent frequency dependence of the properties of velocity discontinuities as predicted by thermodynamic analyses [*Helffrich and Bina*, 1994; *Stixrude*, 1997]. Thus the apparent magnitude of the seismic discontinuity may not provide robust constraints on the olivine content. What is needed is careful comparison between regional

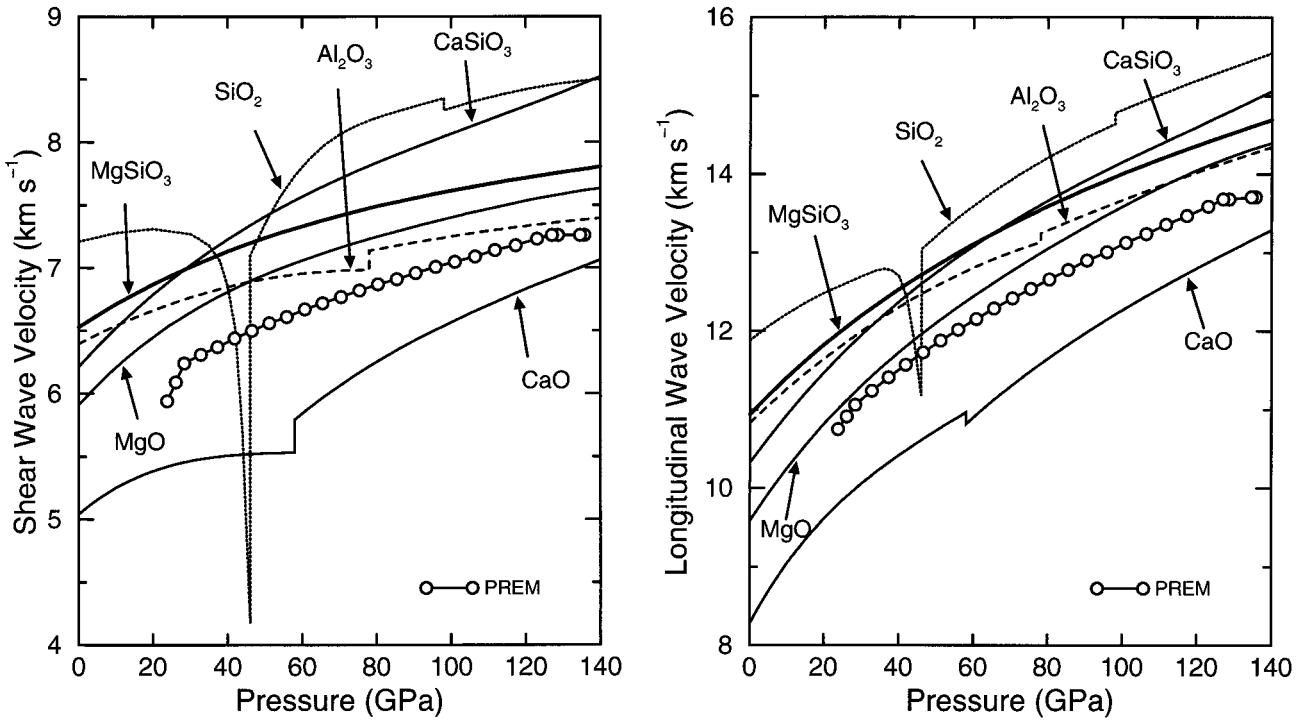

Figure 16. Comparisons of the calculated longitudinal (P) and shear (S) wave velocities of major silicates and oxides ($MgSiO_3$ perovskite [*Karki et al.*, 1997c]; MgO [*Karki et al.*, 1997a]; $CaSiO_3$ perovskite [*Karki and Crain*, 1998a]; high-pressure polymorphs of SiO_2 [*Karki et al.*, 1997d]; CaO [*Karki and Crain*, 1998b]; and Al_2O_3 [*Duan et al.*, 1999]) with the seismic data of the lower mantle given by the PREM [*Dziewonski and Anderson*, 1981].

seismic velocity models and elastic constants determined along geotherms and for bulk compositions appropriate for that region. Nevertheless, the seismologically determined velocity jump appears to be systematically smaller than that of the olivine-to-wadsleyite transition. This indicates that the mantle is not pure olivine. This conclusion is consistent with a broad range of compositional models of the mantle including pyrolite and piclogite.

Karki and Stixrude [1999] have presented comprehensive comparisons of the calculated velocities of silicates and oxides with seismic properties of the lower mantle, focusing on two central issues of the composition of this region: its dominant mineralogy and the detectability of secondary and minor phases (Figure 16). The athermal velocity profiles of $MgSiO_3$ perovskite are nearly parallel to and are higher than those of the lower mantle [*Dziewonski and Anderson*, 1981]. The fact that the velocity profiles of $MgSiO_3$ perovskite are nearly parallel and shifted upward by a few percent (8–10%) with respect to the seismic profiles indicates that perovskite is indeed the dominant phase in the lower mantle [*Karki et al.*, 1997c; *Karki and Stixrude*, 1999]. The differences can be attributed to the effects of iron and high temperatures in the lower mantle and to contributions from the secondary phases such as magnesiowüstite and $CaSiO_3$ perovskite. This picture has been supported in the past by only a limited subset of seismological observations (density and bulk sound velocity). The first-principles studies show that V_P and V_S are also consistent with the perovskite-rich lower mantle hypothesis. This is significant because the P and S wave velocities are expected to be more sensitive to bulk composition and mineral structure than are density and bulk modulus. However, the lack of sufficient information regarding the effects of high temperature and composition do not yet permit us uniquely to resolve the composition and mineralogy of the lower mantle. In particular, it is not yet possible on the basis of first-principles calculations to distinguish pyrolite from the more iron- or silica-rich compositions that have been proposed [*Jeanloz and Knittle*, 1989; *Stixrude et al.*, 1992; *Zhao and Anderson*, 1994].

The density and bulk sound velocity profiles of $CaSiO_3$ perovskite are nearly identical with those of (Mg,Fe) SiO_3 perovskite with ~10% iron. This has led to the suggestion that $CaSiO_3$ perovskite would be a seismically invisible component of the lower mantle [*Mao et al.*, 1989; *Wang et al.*, 1996]. However, theoretical calculations of *Karki and Crain* [1998a] of the shear wave velocity of $CaSiO_3$ perovskite do not support this view. The calculations show that V_S of $CaSiO_3$ perovskite is substantially higher than that of Mg-rich silicate perovskite in the deep lower mantle. Another potential minor phase in the lower mantle, silica, also has distinctive seismic properties. The calculated velocities of silica are substantially higher than the seismic observations (by as much as 20% in V_S) [*Karki et al.*, 1997d]. Moreover,

in the neighborhood of the stishovite-to-$CaCl_2$ phase transition, due to the tetragonal shear instability, the P and S velocities decrease by 20 and 60%, respectively. This indicates that if free silica exists in the lower mantle, it should lead to an observable seismic discontinuity near a depth of 1180 km. Thus, among the candidate phases generally considered for the lower mantle, none are invisible (Figure 16).

4.4.2. Lateral heterogeneity. Seismic tomography has revealed significant lateral variations in velocities throughout the mantle [*van der Hilst et al*., 1991; *Robertson and Woodhouse*, 1996]. The lateral heterogeneity can, in general, be associated with lateral variations in temperature, composition, or phase. In the transition zone, lateral variations in phase assemblage, due to temperature-induced phase transformations [*Anderson*, 1987], are expected to be particularly important. An example of such a transition is that from garnet to ilmenite, which would be expected as one moves from normal mantle into a cold subduction environment. The large contrast in velocity between two phases (10% in V_S) may contribute substantially to the observed lateral velocity structure in the transition zone [*da Silva et al*., 1997].

Lateral variations in composition including variations in Fe/(Fe + Mg), Si/(Mg + Si), or Ca/(Ca + Mg) ratios may be relevant for the lower mantle. The lateral heterogeneity may be characterized by the ratio $\nu = \Delta \ln V_S/\Delta \ln V_P$, whose seismic value varies from 1.7 to 3 across the lower mantle [*Robertson and Woodhouse*, 1996]. A change in the Fe/(Fe + Mg) ratio that affects the shear modulus selectively with negligible effect on the bulk modulus should give ν in the range of 1–1.5, as estimated from the experimental data [*Duffy and Anderson*, 1989]. One can calculate the effect of variation in Si/(Mg + Si) by comparing wave velocities of $MgSiO_3$ perovskite and MgO (Figure 16) to give $\nu \sim 1.2$. However, a variation in the Ca/(Ca + Mg) ratio can make ν as high as 4 because the shear velocity of $CaSiO_3$ perovskite is much higher than that of $MgSiO_3$ perovskite, whereas their longitudinal velocities are similar in the lower mantle (Figure 16). Lateral variations in temperature must also contribute to lateral heterogeneity in the lower mantle. Several studies have shown that the effect of temperature on V_P and V_S changes with pressure in such a way that ν increases with depth [*Karki et al*., 1999; *Isaak et al*., 1992]. Thermal anomalies alone appear unable to account for the observed seismic heterogeneity at the bottom of the lower mantle [*Karato and Karki*, 2001].

4.4.3. Seismic anisotropy. Seismic anisotropy, a measure of the variation of seismic wave velocities with propagation or polarization direction, represents an additional dimension in relating seismological observations to geodynamical and tectonic processes. Among several factors that have made the interpretation of the observed anisotropy difficult has been the lack of information about the elastic constants and anisotropy of constituent minerals at geophysically relevant conditions. Once these are known, the anisotropy of an aggregate is then determined by the lattice-preferred orientation (LPO) of its components or the shape-preferred orientation (SPO) of aligned inclusions with distinct elastic moduli [see *Karato*, 1998b].

The seismic anisotropy in the upper mantle, confirmed by several independent observations of body and surface waves [see, e.g., *Montagner*, 1998; *Mainprice et al*., 2000], has long been thought to be due to the flow-induced lattice-preferred orientation in olivine polycrystal [*Ribe*, 1989]. This is consistent with the strong anisotropy of olivine experimentally and theoretically determined at high pressure [*Zha et al*., 1998; *da Silva et al*., 1997] and the experimentally observed deformation mechanisms in this mineral.

The transition zone shows a transverse (radial) anisotropy with $V_{SH} > V_{SV}$. Wadsleyite may be responsible for the observed anisotropy in the upper part of the transition zone: It is the most abundant mineral in this depth range and is found to be highly anisotropic [*Kiefer et al*., 2001]. On the other hand, in the lower part of the transition zone, the likely major minerals, spinel and garnet, show weak anisotropy (1–2%) at high pressures [*Kiefer et al*., 1997; *Chai and Brown*, 1997]. The observed anisotropy in this region, as suggested by *Karato* [1998b], may require contributions from SPO associated with the large contrast in the elastic moduli of these phases.

Significant seismic anisotropy has been reported in the top and bottom few hundred kilometers of the lower mantle [*Montagner and Kennett*, 1996; *Kendall and Silver*, 1996; *Garnero and Lay*, 1997; *Lay et al*., 1998], while the bulk of this region appears to be isotropic [*Kaneshima and Silver*, 1995; *Meade et al*., 1995]. Recently, theoretically predicted elastic constants of $MgSiO_3$ perovskite and MgO have been used to investigate the possible origins of anisotropy in the lower mantle [*Karato*, 1998a, 1998b; *Stixrude*, 1999]. This remains an uncertain exercise, because in contrast to the situation in the upper mantle, we currently have no information regarding the deformation mechanisms of lower mantle minerals at the relevant pressures. The nature of the LPO that is likely to develop in lower mantle aggregates critically influences the sense of the seismic anisotropy. For example, if the easiest glide plane in $MgSiO_3$ perovskite is (010), as it is in analog $CaTiO_3$ perovskite [*Karato*, 1998b], then polycrystalline perovskite aggregates show $V_{SV} > V_{SH}$ (with (010) horizontal) (Figure 17). However, if (100) is the easiest glide plane, as suggested by the ratio of c_{55}/c_{44} at high pressure, then the sense of anisotropy is reversed. The dominant glide plane in MgO is likely to change from the {110} to {100} plane in the deep lower mantle because with increasing pressure c_{44} corresponding to the shear along the {100} plane becomes increasingly smaller than $(c_{11} - c_{12})/2$, which corresponds to the shear along the {110} plane [*Karato*, 1998a]. The {100} glide results in $V_{SH} > V_{SV}$

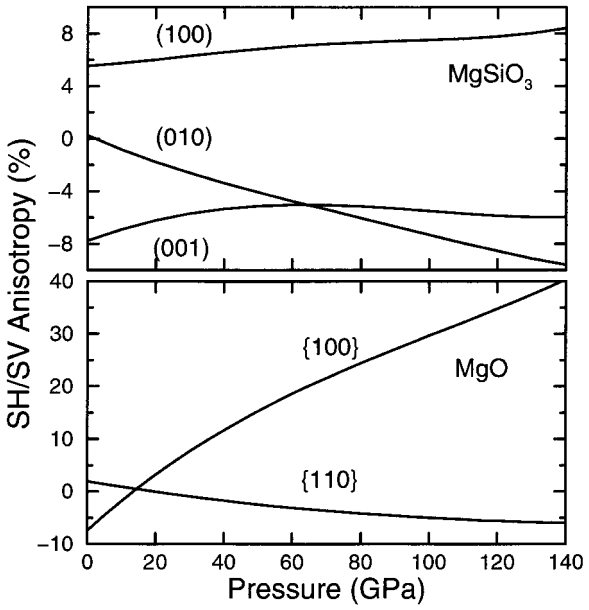

Figure 17. The SH/SV anisotropy for monophase aggregates of $MgSiO_3$ perovskite and MgO due to the lattice-preferred orientations with glide planes as shown, calculated using the elastic moduli from *Karki et al*. [1997a] and *Karki et al*. [1997c] (SH and SV represent horizontally and vertically polarized shear waves, respectively). Similar behavior has been predicted by subsequent calculations [*Wentzcovitch et al*., 1998b; *Karki et al*., 1999].

anisotropy, whereas the {110} glide yields the opposite sense (Figure 17).

Comparing these results with seismology is further complicated by the spatial variability of anisotropy in the *D″* layer. While $V_{SH} > V_{SV}$ is most frequently observed (in the circum- and central-Pacific regions), $V_{SV} > V_{SH}$ is also reported below the central Pacific [*Kendall and Silver*, 1996; *Garnero and Lay*, 1997; *Lay et al*., 1998]. There may be multiple sources of anisotropy at the base of the mantle including LPO and contributions from shape-preferred orientation. The single-crystal anisotropy of both perovskite and MgO are strong enough to cause seismically detectable anisotropy throughout the bulk lower mantle. Similarly, other component minerals including SiO_2 and $CaSiO_3$ perovskite also possess significant anisotropy. The absence of seismic anisotropy in the bulk of the lower mantle requires that LPO be weak or absent in this region, implying a different mechanism of deformation from that operative in the dynamical boundary layers [*Karato*, 1998b; *Meade et al*., 1995].

5. FUTURE PROSPECTS

First-principles methods hold tremendous promise for exploring materials behavior at the extreme conditions that prevail in the deep interior. There is much still to be learned about Earth materials and how their properties control the structure and dynamics of inner Earth. Only a subset of end-member phases have so far been studied from first-principles, but more complex phases such as solid solutions (alloys) with Mg-, Fe-, Ca-, or Al-bearing species are relevant. Computational alchemy or cluster expansion methods have been traditionally used in ab initio studies of semiconductor and metallic alloys and could eventually be applied to oxide and silicate phases as well [*de Gironcoli et al*., 1991; *Saitta et al*., 1998; *Wolverton and Zunger*, 1995].

First-principles calculations have focused to date on the dominant effects of pressure on material properties in the Earth's interior. However, it is only when thermal effects are also fully considered that we will be able to address issues such as the bulk composition of the lower mantle and the origin of the lateral heterogeneity in thermal, compositional, and petrologic contributions and finally to better understand the dynamics of the mantle. Unlike the case of high pressure, primarily because temperature breaks crystal symmetry, finite temperature studies involve relatively large scale computations such as molecular dynamics simulations of large supercells or determination of entire vibrational spectrum that are now becoming feasible within the framework of density functional theory [e.g., *Baroni et al*., 1987; *Karki et al*., 1999; *Alfe et al*., 2000].

Though stresses are expected to be nearly hydrostatic in most of the Earth's interior, there are regions such as boundary layers where shear strain is large and persistent. The Earth is a multiphase composite with properties dependent on textures, deformations, dislocations, slip systems, flow patterns, and other rheological features that are sensitive to both stress and temperature conditions. Yet to be explored are the nature of transport phenomena (diffusion, viscosity), heterogeneous structures (solid/melt interfaces), and defects at high pressure. All these properties involve large-scale molecular dynamics simulations that have so far been tractable only with interatomic potentials or simplified physical models [e.g., *Ita and Cohen*, 1997]. First-principles studies in these areas represent exciting future directions in mineral physics and solid Earth geophysics.

ACKNOWLEDGMENTS. This research was supported by the Minnesota Supercomputer Institute and the National Science Foundation under grants EAR-9628199, EAR-9628042, and EAR-9973139.

Roel Snieder and Thomas Torgersen were the Editors responsible for this paper. They thank Pierre Vacher and David Price for technical reviews and an anonymous cross-disciplinary reviewer.

REFERENCES

Aki, K., and P. G. Richards, *Quantitative Seismology: Theory and Methods*, vol. 2, W. H. Freeman, New York, 1980.

Alfe, D., G. Kresse, and M. J. Gillan, Structure and dynamics

of liquid iron under Earth's core conditions, *Phys. Rev. B*, *61*, 132–142, 2000.
Anderson, D. L., Thermally induced phase changes, lateral heterogeneity of the mantle, continental roots, and deep slab anomalies, *J. Geophys. Res*., *92*, 13,968–13,980, 1987.
Anderson, D. L., and J. W. Given, Absorption-band Q model for the Earth, *J. Geophys. Res*., *87*, 3893–3904, 1982.
Anderson, O. K., Linear methods in band theory, *Phys. Rev. B*, *12*, 3060–3083, 1975.
Anderson, O. L., D. Isaak, and H. Oda, High-temperature elastic constant data on minerals relevant to geophysics, *Rev. Geophys*., *30*, 57–90, 1992.
Andrault, D., G. Fiquet, F. Guyot, and M. Hanfland, Pressure-induced Landau-type transition in stishovite, *Science*, *282*, 720–724, 1998.
Backus, G. E., Long-wave elastic anisotropy produced by horizontal layering, *J. Geophys. Res*., *67*, 4427–4440, 1962.
Bagno, P., O. Jepsen, and O. Gunnarsson, Ground-state properties of 3rd-row elements with nonlocal density functionals, *Phys. Rev. B*, *40*, 1997–2000, 1989.
Baroni, S., P. Giannozzi, and A. Testa, Green's-function approach to linear response in solid, *Phys. Rev. Lett*., *58*, 1861–1864, 1987.
Barron, T. H. K., and M. L. Klein, Second-order elastic constants of a solid under stress, *Proc. Phys. Soc*., *85*, 523–532, 1965.
Bass, J. D., R. C. Liebermann, D. J. Weidner, and S. J. Finch, Elastic properties from acoustic and volume compression experiments, *Phys. Earth Planet. Inter*., *25*, 140–158, 1981.
Birch, F., The effect of pressure upon the elastic parameters of isotropic solids, according to Murnaghan's theory of theory of finite strain, *J. Appl. Phys*., *9*, 279–288, 1938.
Birch, F., Elasticity and constitution of the Earth's interior, *J. Geophys. Res*., *57*, 227–286, 1952.
Birch, F., The velocity of compressional waves in rocks to 10 kilobars, part 2, *J. Geophys. Res*., *66*, 2199–2224, 1961.
Bukowinski, M. S. T., Quantum geophysics, *Annu. Rev. Earth Planet. Sci*., *22*, 167–205, 1984.
Bukowinski, M. S. T., First principles equations of state of MgO and CaO, *Geophys. Res. Lett*., *12*, 536–539, 1985.
Bunge, H. J., *Texture Analysis in Materials Sciences*, Butterworths, London, 1982.
Campbell, A. J., and D. L. Heinz, A high pressure test of Birch law, *Science*, *257*, 66–68, 1992.
Car, R., and M. Parrinello, Unified approach for molecular dynamics and density functional theory, *Phys. Rev. Lett*., *55*, 2471–2474, 1985.
Ceperley, D. M., and B. J. Alder, Ground state of the electron gas by a stochastic method, *Phys. Rev. Lett*., *45*, 566–569, 1980.
Chai, M., and J. M. Brown, The elastic constants of a pyrope-grossular-almandine garnet to 20 GPa, *Geophys. Res. Lett*., *24*, 523–526, 1997.
Chang, P., and E. K. Graham, Elastic properties of oxides in the NaCl structure, *J. Phys. Chem. Solids*, *38*, 1355–1362, 1977.
Christensen, N. I., and M. H. Salisbury, Seismic anisotropy in the oceanic upper mantle: Evidence from the Bay of Islands ophiolite complex, *J. Geophys. Res*., *84*, 4601–4610, 1979.
Cohen, A. J., and R. J. Gordon, Modified electron-gas study of the stability, elastic properties and high-pressure behavior of MgO and CaO crystal, *Phys. Rev. B Solid State*, *14*, 4593–4605, 1976.
Cohen, M. L., and V. Heine, The fitting of pseudopotentials to experimental data and their subsequent application, *Solid State Phys*., *24*, 238–249, 1970.
Cohen, R. E., Calculation of elasticity and high-pressure instabilities in corundum and stishovite with the potential induced breathing model, *Geophys. Res. Lett*., *14*, 37–40, 1987a.
Cohen, R. E., Elasticity and equation of state of $MgSiO_3$-perovskite, *Geophys. Res. Lett*., *14*, 1053–1056, 1987b.
Cohen, R. E., Bonding and elasticity of stishovite SiO_2 at high pressure: Linearised augmented plane wave calculations, *Am. Mineral*., *76*, 733–742, 1991.
Cohen, R. E., First-principles predictions of elasticity and phase transitions in high pressure SiO_2 and geophysical implications, in *High-Pressure Research: Application to Earth and Planetary Sciences*, *Geophys. Monogr. Ser*., vol. 67, edited by Y. Syono and M. H. Manghnani, pp. 425–431, AGU, Washington, D. C., 1992.
Dahlen, F. A., and J. Tromp, *Theoretical Global Seismology*, Princeton Univ. Press, Princeton, N. J., 1998.
da Silva, C., L. Stixrude, and R. M. Wentzcovitch, Elastic constants and anisotropy of fosterite at high pressure, *Geophys. Res. Lett*., *24*, 1963–1966, 1997.
da Silva, C., B. B. Karki, L. Stixrude, and R. M. Wentzcovitch, Ab initio study of the elastic behavior of $MgSiO_3$ ilmenite at high pressure, *Geophys. Res. Lett*., *26*, 943–946, 1999.
Davies, G. F., Effective elastic moduli under hydrostatic stress, I, Quasi-harmonic theory, *J. Phys. Chem. Solids*, *35*, 1513–1520, 1974.
de Gironcoli, S., P. Gianozzi, and S. Baroni, Structure and thermodynamics of Si_xGe-1.x alloys from ab initio Monte Carlo simulations, *Phys. Rev. Lett*., *66*, 2116–2119, 1991.
Demuth, T., Y. Jeanvoine, J. Hafner, and J. G. Angyan, Polymorphism in silica studied in the local density and generalized-gradient approximations, *J. Phys. Condens. Matter*, *11*, 3833–3874, 1999.
Dovesi, R., R. Orlando, C. Roetti, C. Pisani, and V. R. Saunders, The periodic Hartree-Fock method and its implementation in the CRYSTAL code, *Phys. Status Solidi B*, *217*, 63–88, 2000.
Duan, W., B. B. Karki, and R. M. Wentzcovitch, High pressure elasticity of alumina studied by first principles, *Am. Mineral*., *84*, 1961–1966, 1999.
Duffy, T. S., and D. L. Anderson, Seismic velocities in mantle minerals and the mineralogy of the upper mantle, *J. Geophys. Res*., *94*, 1895–1912, 1989.
Duffy, T. S., R. J. Hemley, and H. K. Mao, Equation of state and shear strength at multimegabar pressures: Magnesium oxide to 227 GPa, *Phys. Rev. Lett*., *74*, 1371–1374, 1995.
Dziewonski, A. M., and D. L. Anderson, Preliminary reference Earth model, *Phys. Earth Planet. Inter*., *25*, 297–356, 1981.
Fujisawa, H., Elastic wave velocities of fosterite and its β-spinel form and chemical boundary hypothesis for the 410-km discontinuity, *J. Geophys. Res*., *103*, 9591–9608, 1998.
Gaherty, J. B., T. H. Jordan, and L. S. Gee, Seismic structure of the upper mantle in a central Pacific corridor, *J. Geophys. Res*., *101*, 22,291–22,309, 1996.
Garnero, E. J., and D. V. Helmberger, Seismic detection of a thin laterally varying boundary layer at the base of the mantle beneath the central Pacific, *Geophys. Res. Lett*., *23*, 977–980, 1996.
Garnero, E. J., and T. Lay, Lateral variation in lowermost mantle shear wave anisotropy beneath the North Pacific and Alaska, *J. Geophys. Res*., *102*, 8121–8135, 1997.
Gieske, J. H., and G. R. Barsch, Pressure dependence of the elastic constants of single crystalline aluminum oxide, *Phys. Status Solidi*, *29*, 121–131, 1968.
Hamann, D. R., Generalized gradient theory for silica phase transitions, *Phys. Rev. Lett*., *76*, 660–663, 1996.
Hamann, D. R., M. Schlüter, and C. Chiang, Norm-conserving pseudopotentials, *Phys. Rev. Lett*., *43*, 1494–1497, 1979.
Hashin, Z., and S. Shtrikman, A variational approach to the

theory of the elastic behavior of polycrystals, *J. Mech. Phys. Solids*, *10*, 343–352, 1962.
Hazen, R. M., and L. W. Finger, Bulk modulus-volume relationship for cation-anion polyhedra, *J. Geophys. Res.*, *84*, 6723–6728, 1979.
Heine, V., The pseudopotential concept, *Solid State Phys.*, *24*, 1–37, 1970.
Helbig, K., *Foundations of Anisotropy for Exploration Seismics*, Pergamon, New York, 1984.
Helffrich, G., and C. R. Bina, Frequency dependence of the visibility and depths of mantle seismic discontinuities, *Geophys. Res. Lett.*, *21*, 2613–2616, 1994.
Hill, R., The elastic behavior of a crystalline aggregate, *Proc. Phys. Soc. London*, *Ser. A*, *65*, 349–354, 1952.
Hohenberg, P., and W. Kohn, Inhomogeneous electron gas, *Phys. Rev. B*, *136*, 864–871, 1964.
Ihm, J., Total energy calculations in solid-state physics, *Rep. Prog. Phys.*, *51*, 105–142, 1988.
Isaak, D. G., R. E. Cohen, and M. E. Mehl, Calculated elastic constants and thermal properties of MgO at high pressures and temperatures, *J. Geophys. Res.*, *95*, 7055–7067, 1990.
Isaak, D. G., O. L. Anderson, and R. E. Cohen, The relationship between shear and compressional velocities at high pressures: Reconciliation of seismic tomography and mineral physics, *Geophys. Res. Lett.*, *19*, 741–744, 1992.
Ishii, M., and J. Tromp, Normal-mode and free-air gravity constraints on lateral variations in velocity and density of Earth's mantle, *Science*, *285*, 1231–1236, 1999.
Ita, J., and R. E. Cohen, Effects of pressure on diffusion and vacancy formation in MgO from nonempirical free-energy integrations, *Phys. Rev. Lett.*, *79*, 3198–3201, 1997.
Jackson, D. D., and D. L. Anderson, Physical mechanisms of seismic-wave attenuation, *Rev. Geophys.*, *8*, 1–63, 1970.
Jansen, H. J. F., and A. J. Freeman, Total-energy full-potential linearized augmented-plane-wave method for bulk solids—Electronic and structural properties of tungsten, *Phys. Rev. B*, *30*, 561–569, 1984.
Jeanloz, R., Universal equation of state, *Phys. Rev. B*, *38*, 805–807, 1988.
Jeanloz, R., and E. Knittle, Density and composition of the lower mantle, *Philos. Trans. R. Soc. London*, *Ser. A*, *238*, 377–389, 1989.
Jeanloz, R., and S. Morris, Temperature distribution in the crust and mantle, *Annu. Rev. Earth Planet. Sci.*, *14*, 377–415, 1986.
Jeanloz, R., and A. Thompson, Phase transitions and mantle discontinuities, *Rev. Geophys.*, *21*, 51–74, 1983.
Jones, R. O., and O. Gunnarsson, The density functional formalism, its applications and prospects, *Rev. Mod. Phys.*, *61*, 689–746, 1989.
Kanamori, H., and D. L. Anderson, Importance of physical dispersion in surface-wave and free-oscillation problems: A review, *Rev. Geophys.*, *15*, 105–112, 1977.
Kaneshima, S., and P. G. Silver, Anisotropic loci in the mantle beneath central Peru, *Phys. Earth Planet. Inter.*, *88*, 257–272, 1995.
Karato, S., Importance of anelasticity in the interpretation of seismic tomography, *Geophys. Res. Lett.*, *20*, 1623–1626, 1993.
Karato, S., Some remarks on the origin of seismic anisotropy in the *D″* layer, *Earth Planets Space*, *50*, 1019–1028, 1998a.
Karato, S., Seismic anisotropy in the deep mantle, boundary layers and the geometry of mantle convection, *Pure Appl. Geophys.*, *151*, 565–587, 1998b.
Karato, S., and B. B. Karki, Origin of lateral variation of seismic wave velocities and density in the deep mantle, *J. Geophys. Res.*, *106*, 21,771–21,783, 2001.
Karato, S., and H. A. Spetzler, Defect microdynamics in minerals and solid-state mechanisms of seismic-wave attenuation and velocity dispersion in the mantle, *Rev. Geophys.*, *28*, 399–421, 1990.
Karki, B. B., High pressure structure and elasticity of the major silicate and oxide minerals of the Earth's lower mantle, Ph.D. thesis, Univ. of Edinburgh, Edinburgh, Scotland, 1997.
Karki, B. B., and J. Crain, First-principles determination of elastic properties of $CaSiO_3$ perovskite at lower mantle pressures, *Geophys. Res. Lett.*, *25*, 2741–2744, 1998a.
Karki, B. B., and J. Crain, Structure and elasticity of CaO at high pressure, *J. Geophys. Res.*, *103*, 12,405–12,411, 1998b.
Karki, B. B., and L. Stixrude, Seismic velocities of major silicate and oxide phases of the lower mantle, *J. Geophys. Res.*, *104*, 13,025–13,033, 1999.
Karki, B. B., L. Stixrude, S. J. Clark, M. C. Warren, G. J. Ackland, and J. Crain, Structure and elasticity of MgO at high pressure, *Am. Mineral.*, *82*, 52–61, 1997a.
Karki, B. B., M. C. Warren, L. Stixrude, G. J. Ackland, and J. Crain, Ab initio studies of high-pressure structural transformations in silica, *Phys. Rev. B*, *55*, 3465–3472, 1997b. (Correction, *Phys. Rev. B*, *56*, 2884, 1997.)
Karki, B. B., L. Stixrude, S. J. Clark, M. C. Warren, G. J. Ackland, and J. Crain, Elastic properties of orthorhombic $MgSiO_3$ perovskite at lower mantle pressures, *Am. Mineral.*, *82*, 635–638, 1997c.
Karki, B. B., L. Stixrude, and J. Crain, Ab initio elasticity of three high-pressure polymorphs of silica, *Geophys. Res. Lett.*, *24*, 3269–3272, 1997d.
Karki, B. B., G. J. Ackland, and J. Crain, Elastic instabilities from ab-initio stress-strain relations, *J. Phys. C*, *9*, 8579–8589, 1997e.
Karki, B. B., R. M. Wentzcovitch, S. de Gironcoli, and S. Baroni, Elastic anisotropy and wave velocities of MgO at lower mantle conditions, *Science*, *286*, 1705–1707, 1999.
Karki, B. B., W. Duan, C. R. S. da Silva, and R. M. Wentzcovitch, Ab initio structure of $MgSiO_3$ ilmenite at high pressure, *Am. Mineral.*, *85*, 317–320, 2000.
Kendall, J. M., and P. G. Silver, Constraints from seismic anisotropy on the nature of the lowermost mantle, *Nature*, *381*, 409–412, 1996.
Kiefer, B., L. Stixrude, and R. M. Wentzcovitch, Calculated elastic constants and anisotropy of Mg_2SiO_4 spinel at high pressure, *Geophys. Res. Lett.*, *24*, 2841–2844, 1997.
Kiefer, B., L. Stixrude, J. Hafner, and G. Kresse, Structure and elasticity of wadsleyite at high pressures, *Am. Mineral.*, in press, 2001.
Knittle, E., and R. Jeanloz, High-pressure X-ray-diffraction and optical-absorption studies of CsI, *J. Phys. Chem. Solids*, *46*, 1179–1184, 1985.
Kohn, W., and L. J. Sham, Self-consistent equations including exchange and correlation effects, *Phys. Rev. A*, *140*, 1133–1138, 1965.
Lay, T., Q. Williams, and E. J. Garnero, The core-mantle boundary layer and deep Earth dynamics, *Nature*, *392*, 461–468, 1998.
Lee, M. H., Advanced pseudopotentials for large scale electronic structure calculations, Ph.D. thesis, Univ. of Cambridge, Cambridge, England, 1995.
Li, B., R. C. Liebermann, and D. J. Weidner, Elastic moduli of wadsleyite (β-Mg_2SiO_4) to 7 gigapascals and 873 Kelvin, *Science*, *281*, 675–677, 1998.
Liebermann, R. C., and B. Li, Elasticity at high pressures and temperatures, *Rev. Mineral.*, *37*, 459–492, 1998.
Lundqvist, S., and N. H. March, *Theory of the Inhomogeneous Electron Gas*, Plenum, New York, 1987.
Mainprice, D., G. Barruol, and W. Ben Ismail, The seismic anisotropy of the Earth's mantle: From single crystal to polycrystal, in *Earth's Deep Interior: Mineral Physics and Tomography From the Atomic to the Global Scale*, *Geophys.*

Monogr. Ser., vol. 117, edited by S. Karato et al., pp. 237–264, AGU, Washington, D. C., 2000.

Mao, H. K., L. C. Chen, R. J. Hemley, A. P. Jephcoat, Y. Wu, and W. A. Bassett, Stability and equation of state of $CaSiO_3$ perovskite to 134 GPa, *J. Geophys. Res*., *94*, 17,889–17,894, 1989.

Masters, G., and P. M. Shearer, Seismic models of the Earth: Elastic and anelastic, in *Global Earth Physics*: *A Handbook of Physical Constants*, *AGU Ref. Shelf Ser*., vol. 1, edited by T. J. Ahrens, pp. 88–103, AGU, Washington, D. C., 1995.

Masters, G., S. Johnson, G. Laske, and H. Bolton, A shear-velocity model of the mantle, *Philos. Trans. R. Astron. Soc. A*, *354*, 1385–1410, 1996.

Matsui, M., M. Akaogi, and T. Matsumoto, Computational model of the structural and elastic properties of the ilmenite and perovskite phases of $MgSiO_3$, *Phys. Chem. Miner*., *14*, 101–106, 1987.

Meade, C., P. G. Silver, and S. Kaneshima, Laboratory and seismological observations of lower mantle isotropy, *Geophys. Res. Lett*., *22*, 1293–1296, 1995.

Mehl, M. J., R. J. Hemley, and L. L. Boyer, Potential-induced breathing model for the elastic moduli and high-pressure behavior of the cubic alkaline-Earth oxides, *Phys. Rev. B Condens. Matter*, *33*, 8685–8696, 1986.

Mehl, M. J., R. E. Cohen, and H. Krakauer, Linearized augmented plane wave electronic structure calculations for MgO and CaO, *J. Geophys. Res*., *93*, 8009–8022, 1988.

Mizushima, K., S. Yip, and E. Kaxiras, Ideal crystal stability and pressure-induced phase transition in silicon, *Phys. Rev. B*, *50*, 14,952–14,959, 1994.

Monkhorst, H. J., and J. D. Pack, Special points for Brillouin-zone integrations, *Phys. Rev. B Solid State*, *13*, 5188–5192, 1976.

Montagner, J. P., Where can seismic anisotropy be detected in the Earth mantle? In boundary layers, *Pure Appl. Geophys*., *151*, 223–256, 1998.

Montagner, J. P., and N. L. N. Kennett, How to reconcile body-wave and normal mode reference Earth model, *Geophys. J. Int*., *125*, 229–248, 1996.

Moruzzi, V. L., J. F. Janak, and A. R. Williams, *Calculated Electronic Properties of Metals*, Pergamon, New York, 1978.

Musgrave, M. J. P., *Crystal Acoustics*, Holden-Day, Boca Raton, Fla., 1970.

Nastar, M., and F. Willaime, Tight-binding calculations of the elastic-constants of fcc and hcp transition metals, *Phys. Rev. B*, *51*, 6896–6907, 1995.

Nielsen, O. H., and R. Martin, Quantum mechanical theory of stress and force, *Phys. Rev. B*, *32*, 3780–3791, 1985.

Nye, J. F., *Physical Properties of Crystals: Their Representation by Tensors and Matrices*, Oxford Univ. Press, New York, 1985.

Oganov, A. R., J. P. Brodholt, and G. D. Price, Ab initio elasticity and thermal equation of state of $MgSiO_3$ perovskite, *Earth Planet. Sci. Lett*., *184*, 555–560, 2001.

Payne, M. C., M. P. Teter, D. C. Allen, T. A. Arias, and J. D. Joannopoulos, Iterative minimisation techniques for ab initio total-energy calculations: Molecular dynamics and conjugate gradients, *Rev. Mod. Phys*., *64*, 1045–1097, 1992.

Perdew, J. P., and A. Zunger, Self-interaction correction to density functional approximations for many-electron systems, *Phys. Rev. B*, *23*, 5048–5079, 1981.

Perdew, J. P., K. Burke, and M. Ernzerhof, Generalized gradient approximation made simple, *Phys. Rev. Lett*., *77*, 3865–3868, 1996.

Pickett, W. E., Pseudopotential methods in condensed matter applications, *Comput. Phys. Rep*., *9*, 115–197, 1989.

Ribe, N. M., Seismic anisotropy and mantle flow, *J. Geophys. Res*., *94*, 4213–4223, 1989.

Rigden, S. M., G. D. Gwanmesia, I. Jackson, and R. C. Liebermann, Progress in high-pressure ultrasonic interferometry, the pressure dependence of elasticity of Mg_2SiO_4 polymorphs, and constraints on composition of the transition zone of the Earth's mantle, in *High Pressure Research: Applications to Earth and Planetary Sciences*, *Geophys. Monogr. Ser*., vol. 67, edited by Y. Syono and M. H. Manghnani, pp. 167–182, AGU, Washington, D. C., 1992.

Rivers, M. L., and I. S. E. Carmichael, Ultrasonic studies of silicate melts, *J. Geophys. Res*., *92*, 9247–9270, 1987.

Robertson, G. S., and J. H. Woodhouse, Ratio of relative *S* to *P* velocity heterogeneity in the lower mantle, *J. Geophys. Res*., *101*, 20,041–20,052, 1996.

Romanowicz, B., Seismic tomography of the Earth's mantle, *Annu. Rev. Earth Planet. Sci*., *19*, 77–99, 1991.

Ruff, L. J., State of stress within the Earth, in *IASPEI Handbook on Earthquake and Engineering Seismology*, edited by W. Lee, H. Kanamori, and P. Jennings, Int. Union of Geod. and Geophys., Toronto, Ont., Canada, in press, 2001.

Saitta, A. M., S. de Gironcoli, and S. Baroni, Structural and electronic properties of a wide-gap quaternary solid solution: (Zn, Mg)(S, Se), *Phys. Rev. Lett*., *80*, 4939–4942, 1998.

Salje, E. K. H., *Phase Transitions in Ferroelastic and Co-Elastic Crystals*, Cambridge Univ. Press, New York, 1990.

Shearer, P. M., Upper mantle seismic discontinuities, in *Earth's Deep Interior: Mineral Physics and Tomography From the Atomic to the Global Scale*, *Geophys. Monogr. Ser*., vol. 117, edited by S. Karato et al., pp. 115–131, AGU, Washington, D. C., 2000.

Sherman, D. M., Equation of state, elastic properties, and stability of $CaSiO_3$ perovskite: First principles (periodic Hartree-Fock) results, *J. Geophys. Res*., *98*, 19,795–19,805, 1993.

Sinelnikov, Y. D., G. Chen, D. R. Neuville, M. T. Vaughan, and R. C. Liebermann, Ultrasonic shear wave velocities of $MgSiO_3$ perovskite at 8 GPa and 800 K and lower mantle composition, *Science*, *281*, 677–679, 1998.

Singh, D. J., *Planewaves, Pseudopotentials, and the LAPW Method*, Kluwer Acad., Norwell, Mass., 1994.

Sinogeikin, S. V., and J. D. Bass, Single-crystal elasticity of MgO at high pressure, *Phys. Rev. B*, *59*, 14,141–14,144, 1999.

Soderlind, P., M. A. Moriarty, and J. M. Willis, First-principles theory of iron up to Earth-core pressures: Structural, vibrational and elastic properties, *Phys. Rev. B*, *53*, 14,063–14,072, 1996.

Steinle-Neumann, G., L. Stixrude, and R. E. Cohen, First principles elastic constants for the hcp transition metals Fe, Co, and Re at high pressure, *Phys. Rev. B*, *60*, 791–799, 1999.

Stixrude, L., Structure and sharpness of phase transitions and mantle discontinuities, *J. Geophys. Res*., *102*, 14,835–14,852, 1997.

Stixrude, L., Elastic constants and anisotropy of $MgSiO_3$ perovskite, periclase, and SiO_2 at high pressure, in *The Core-Mantle Boundary Region*, *Geodyn. Ser*., vol. 28, edited by M. Gurnis et al., pp. 83–96, AGU, Washington, D. C., 1999.

Stixrude, L., and R. E. Cohen, Stability of orthorhombic $MgSiO_3$-perovskite in the Earth's lower mantle, *Nature*, *364*, 613–616, 1993.

Stixrude, L., R. J. Hemley, Y. Fei, and H.-K. Mao, Thermoelasticity of silicate perovskite and magnesiowüstite and the stratification of the Earth's mantle, *Science*, *257*, 1099–1101, 1992.

Stixrude, L., R. E. Cohen, and D. J. Singh, Iron at high pressure: Linearized augmented plane wave calculations in the generalized gradient approximation, *Phys. Rev. B*, *50*, 6442–6445, 1994.

Stixrude, L., R. E. Cohen, and R. J. Hemley, Theory of minerals at high pressure, *Rev. Mineral*., *37*, 639–671, 1998.

Tang, M., and S. Yip, Atomic size effects in pressure-induced amorphization of a binary covalent lattice, *Phys. Rev. Lett*., *75*, 2738–2741, 1995.

Troullier, N., and J. L. Martins, Efficient pseudopotentials for plane-wave calculations, *Phys. Rev. B*, *43*, 1993–2003, 1991.

Turcotte, D. L., and G. Schubert, *Geodynamics*, John Wiley, New York, 1982.

Vanderbilt, D., Soft self-consistent pseudopotentials in a generalized eigenvalue formalism, *Phys. Rev. B*, *41*, 7892–7895, 1990.

van der Hilst, R., and H. Karason, Compositional heterogeneity in the bottom 1000 kilometers of Earth's mantle: Toward a hybrid convection model, *Science*, *283*, 1885–1888, 1999.

van der Hilst, R., R. Engdahl, W. Spakman, and G. Nolet, Tomographic imaging of subducted lithosphere below northwest Pacific island arcs, *Nature*, *353*, 37–43, 1991.

van der Hilst, R., S. Widiyantoro, and E. R. Engdahl, Evidence for deep mantle circulation from global tomography, *Nature*, *386*, 578–584, 1997.

Wallace, D. C., *Thermodynamics of Crystals*, John Wiley, New York, 1972.

Wang, J., S. Yip, S. R. Phillpot, and D. Wolf, Mechanical instabilities in homogeneous crystals, *Phys. Rev. B*, *52*, 12,627–12,635, 1995.

Wang, Y., D. J. Weidner, and F. Guyot, Thermal equation of state of $CaSiO_3$ perovskite, *J. Geophys. Res*., *101*, 661–672, 1996.

Watt, J. P., Polyxstal: A fortran program to calculate average elastic properties of minerals from single-crystal elasticity data, *Comput. Geosci*., *13*, 441–462, 1987.

Watt, J. P., G. F. Davies, and R. J. O'Connell, The elastic properties of composite materials, *Rev. Geophys*., *14*, 541–563, 1976.

Wei, S. H., and H. Krakauer, Local density functional calculation of pressure induced metalization of BaSe and BaTe, *Phys. Rev. Lett*., *55*, 1200–1203, 1985.

Weidner, D. J., A mineral physics test of a pyrolite mantle, *Geophys. Res. Lett*., *12*, 417–420, 1985.

Weidner, D. J., and E. Ito, Elasticity of $MgSiO_3$ in the ilmenite phase, *Phys. Earth Planet. Inter*., *40*, 65–70, 1985.

Weidner, D. J., and M. T. Vaughan, Elasticity of pyroxenes: Effects of composition versus crystal structure, *J. Geophys. Res*., *87*, 9349–9353, 1982.

Weidner, D. J., J. D. Bass, A. E. Ringwood, and W. Sinclair, The single-crystal elastic moduli of stishovite, *J. Geophys. Res*., *87*, 4740–4746, 1982.

Weidner, D. J., H. Sawamoto, S. Sasaki, and M. Kumazawa, Single-crystal elastic properties of the spinel phase of Mg_2SiO_4, *J. Geophys. Res*., *89*, 7852–7860, 1984.

Wenk, H.-R. (Ed.), *Preferred Orientation in Deformed Metals and Rocks: An Introduction to Modern Texture Analysis*, Academic, San Diego, Calif., 1985.

Wentzcovitch, R. M., Invariant molecular dynamics approach to structural phase transitions, *Phys. Rev. B*, *44*, 2358–2361, 1991.

Wentzcovitch, R. M., and J. L. Martins, First principles molecular dynamics of Li: Test of a new algorithm, *Solid State Commun*., *78*, 831–834, 1991.

Wentzcovitch, R. M., and G. D. Price, High pressure studies of mantle minerals by ab initio variable cell shape molecular dynamics, in *Molecular Engineering*, edited by B. Silvi and P. Darco, pp. 39–61, Kluwer Acad., Norwell, Mass., 1996.

Wentzcovitch, R. M., J. L. Martins, and G. D. Price, Ab initio molecular dynamics with variable cell shape: Application to $MgSiO_3$ perovskite, *Phys. Rev. Lett*., *70*, 3947–3950, 1993.

Wentzcovitch, R. M., N. Ross, and G. D. Price, Ab initio study of $MgSiO_3$ and $CaSiO_3$ perovskites at lower mantle conditions, *Phys. Earth Planet. Inter*., *90*, 101–112, 1995a.

Wentzcovitch, R. M., D. A. Hugh-Jones, R. J. Angel, and G. D. Price, Ab initio study of $MgSiO_3$ C2/c enstatite, *Phys. Chem. Miner*., *22*, 453–460, 1995b.

Wentzcovitch, R. M., C. R. S. Da Silva, J. R. Chelikowsky, and N. Binggeli, Phase transition in quartz near the amorphization transformation, *Phys. Rev. Lett*., *80*, 2149–2152, 1998a.

Wentzcovitch, R. M., B. B. Karki, S. Karato, and C. R. S. da Silva, High pressure elastic anisotropy of $MgSiO_3$ perovskite and geophysical implications, *Earth Planet. Sci. Lett*., *164*, 371–378, 1998b.

Wolverton, C., and A. Zunger, Ising-like description of structurally relaxed ordered and disordered alloy, *Phys. Rev. Lett*., *75*, 3162–3165, 1995.

Yaganeh-Haeri, A., Synthesis and re-investigation of the elastic properties of single-crystal magnesium silicate perovskite, *Phys. Earth Planet. Inter*., *87*, 111–121, 1994.

Yoneda, A., and M. Morioka, Pressure derivatives of elastic constants of single crystal forsterite, in *High Pressure Research: Applications to Earth and Planetary Sciences*, *Geophys. Monogr. Ser*., vol. 67, edited by Y. Syono and M. H. Munghnani, pp. 207–214, AGU, Washington, D. C., 1992.

Zha, C.-S., T. S. Duffy, R. T. Downs, H.-K. Mao, and R. J. Hemley, Sound velocity and elasticity of single-crystal forsterite to 16 GPa, *J. Geophys. Res*., *101*, 17,535–17,546, 1996.

Zha, C.-S., T. S. Duffy, R. T. Downs, H. K. Mao, R. J. Hemley, and D. J. Weidner, Single-crystal elasticity of β-Mg_2SiO_4 to pressure of the 410 km seismic discontinuity in the Earth's mantle, *Earth Planet. Sci. Lett*., *147*, E9–E15, 1997.

Zha, C.-S., T. S. Duffy, R. T. Downs, H. K. Mao, and R. J. Hemley, Brillouin scattering and X-ray diffraction of San Carlos olivine: Direct pressure determination to 32 GPa, *Earth Planet. Sci. Lett*., *159*, 25–33, 1998.

Zha, C.-S., H. K. Mao, and R. J. Hemley, Elasticity of MgO and a primary pressure scale to 55 GPa, *Proc. Natl. Acad. Sci*., *97*, 13,494–13,499, 2000.

Zhao, Y. S., and D. L. Anderson, Mineral physics constraints on the chemical composition of the Earth's lower mantle, *Phys. Earth Planet. Inter*., *85*, 273–292, 1994.

B. B. Karki, Department of Physics and Astronomy, Louisiana State University, Baton Rouge, LA 70803-4001, USA. (karki@phys.lsu.edu)

L. Stixrude, Department of Geological Sciences, University of Michigan, 425 East University Avenue, Ann Arbor, MI 48109-1063, USA. (stixrude@umich.edu)

R. M. Wentzcovitch, Department of Chemical Engineering and Materials Science, University of Minnesota, 421 Washington Avenue, SE, Minneapolis, MN 55455, USA. (wentzcov@cems.umn.edu)